Future Changes in Tropical Cyclone Activity Projected by the New High-Resolution MRI-AGCM*

HIROYUKI MURAKAMI

Japan Agency for Marine-Earth Science and Technology, Meteorological Research Institute, Tsukuba, Ibaraki, Japan

YUQING WANG

Department of Meteorology, and International Pacific Research Center, University of Hawaii at Manoa, Honolulu, Hawaii

HIROMASA YOSHIMURA AND RYO MIZUTA

Meteorological Research Institute, Tsukuba, Ibaraki, Japan

MASATO SUGI

Japan Agency for Marine-Earth Science and Technology, Meteorological Research Institute, Tsukuba, Ibaraki, Japan

EIKI SHINDO, YUKIMASA ADACHI, SEIJI YUKIMOTO, MASAHIRO HOSAKA, SHOJI KUSUNOKI, TOMOAKI OSE, AND AKIO KITOH

Meteorological Research Institute, Tsukuba, Ibaraki, Japan

(Manuscript received 3 August 2011, in final form 31 October 2011)

ABSTRACT

New versions of the high-resolution 20- and 60-km-mesh Meteorological Research Institute (MRI) atmospheric general circulation models (MRI-AGCM version 3.2) have been developed and used to investigate potential future changes in tropical cyclone (TC) activity. Compared with the previous version (version 3.1), version 3.2 yields a more realistic simulation of the present-day (1979–2003) global distribution of TCs. Moreover, the 20-km-mesh model version 3.2 is able to simulate extremely intense TCs (categories 4 and 5), which is the first time a global climate model has been able to simulate such extremely intense TCs through a multidecadal simulation. Future (2075–99) projections under the Intergovernmental Panel on Climate Change (IPCC) A1B scenario are conducted using versions 3.1 and 3.2, showing consistent decreases in the number of TCs globally and in both hemispheres as climate warms. Although projected future changes in basin-scale TC numbers show some differences between the two versions, the projected frequency of TC occurrence shows a consistent decrease in the western part of the western North Pacific (WNP) and in the South Pacific Ocean (SPO), while it shows a marked increase in the central Pacific. Both versions project a future increase in the frequency of intense TCs globally; however, the degree of increase is smaller in version 3.2 than in version 3.1. This difference arises partly because version 3.2 projects a pronounced decrease in mean TC intensity in the SPO. The 20-km-mesh model version 3.2 projects a northward shift in the most intense TCs (category 5) in the WNP, indicating an increasing potential for future catastrophic damage due to TCs in this region.

1. Introduction

The potential impacts of global warming (GW) on tropical cyclone (TC) activity have been the subject of much scientific debate in recent years. Many studies have attempted to address future changes in TC activity, including the genesis number, frequency of occurrence, and intensity of TCs [see Knutson et al. (2010a) for a recent review]. Although theory (Emanuel 1987) and a number

* International Pacific Research Center Publication Number 847.

Corresponding author address: Hiroyuki Murakami, JAMSTEC, Meteorological Research Institute, 1-1, Nagamine, Tsukuba, Ibaraki 305-0052, Japan.
E-mail: hir.murakami@gmail.com

DOI: 10.1175/JCLI-D-11-00415.1

of previous studies using state-of-the-art models have suggested that TC intensity would increase and global TC number would decrease with global warming (e.g., Sugi et al. 2002; Emanuel et al. 2008; Gualdi et al. 2008; Zhao et al. 2009; Murakami and Sugi 2010), projected changes in the TC genesis number are highly variable at the ocean basin scale (Emanuel et al. 2008; Zhao et al. 2009; Knutson et al. 2010a). This lack of consensus is reflected in the Intergovernmental Panel on Climate Change (IPCC) Fourth Assessment Report (Solomon et al. 2007), which, in its chapter titled ''Summary for Policymakers'' (Alley et al. 2007), expressed ''less confidence'' in projections of a global decrease in the frequency of TCs than in projections of an increase in maximum intensities. The most recent review papers by Knutson et al. (2010a,b) report that existing modeling studies consistently project decreases in the frequency of global TCs; however, projected changes for individual basins vary substantially among modeling studies.

The uncertainties in the projected future changes in regional TC activity arise from a number of factors, including biases associated with differences in model physics (Yokoi and Takayabu 2009; Yokoi et al. 2009; Murakami et al. 2011), model resolution (Bengtsson et al. 2007; Murakami and Sugi 2010), the chosen global warming scenario (Stowasser et al. 2007), and the assumed spatial pattern of future changes in sea surface temperature (SST) (Sugi et al. 2009; Zhao et al. 2009; Murakami et al. 2011). Bengtsson et al. (2007) reported that projected future changes in the frequency of TC occurrence differ between a model with relatively high spatial resolution (T213) and a model with relatively low spatial resolution (T63). High-resolution models produce much more realistic TC intensities, suggesting that such models may provide more accurate projections of potential changes in TC activity under global warming. Only high-resolution models (60-km mesh or finer) project an increase in TC intensity as climate warms (Knutson et al. 2010a; Murakami and Sugi 2010).

Murakami and Wang (2010) and Murakami et al. (2012) recently investigated future changes in TC activity in the North Atlantic (NAT) and the western North Pacific (WNP), respectively, using the high-resolution Meteorological Research Institute (MRI) atmospheric general circulation model (AGCM) version 3.1 (MRI-AGCM3.1), employing a high resolution with a 20-km mesh. They did not discuss the uncertainties in their projections, however, because high-resolution projections are still computationally expensive, so only limited multimodel or multi-SST ensemble simulations can be conducted.

Given the fact that model biases reduce the reliability of future projections, it is important to minimize such biases. Murakami and Sugi (2010) showed that the 20-km-mesh MRI-AGCM3.1 severely underestimates both the TC intensity and TC genesis frequency (TGF) in the WNP. The latest revision with the replacements of some physical parameterizations has improved the model performance and reduced the model biases (Mizuta et al. 2012). In particular, the replacement of the cumulus convection scheme has contributed to marked improvements in the new version of the model (MRI-AGCM3.2).

In the present study, we used the MRI-AGCM3.2 to simulate both the present-day (PD) climate (1979–2003) and projected climate at the end of the twenty-first century (2075–99) under the IPCC A1B scenario (Solomon et al. 2007). The results of these simulations are used to investigate potential future changes in TC activity at global and regional scales. Results from the previous version of the MRI-AGCM (version 3.1) with 20-km horizontal resolution and from both versions of the MRI-AGCM (versions 3.1 and 3.2) with 60-km horizontal resolution are also used for comparison with the current version to address the uncertainties induced by differences in both model physics and model resolution. This study does not address uncertainties in either the choice of global warming scenario or the assumption of a specific spatial pattern of future changes in SST. These uncertainties are discussed in Murakami et al. (2011).

The remainder of this paper is organized as follows. Section 2 briefly describes the models, experimental design, and analysis methods. Section 3 assesses present-day simulations using different versions and different resolutions of the model. Section 4 presents projected future changes in TC activity, and section 5 discusses the physical mechanisms behind the projected future changes in the TC genesis frequency. Finally, section 6 provides a summary of the results.

2. Methods

a. Models

The models used in this study comprise two versions of MRI-AGCM: 3.1 and 3.2. MRI-AGCM3.1 is based on a global model developed by the Japan Meteorological Agency (JMA) and MRI (Mizuta et al. 2006), and was previously used for the 20-km-resolution climate projections reported in Kitoh et al. (2009). These projections were used to address potential future changes in extreme events, such as TCs (Oouchi et al. 2006; Sugi et al. 2009; Murakami and Sugi 2010; Murakami and Wang 2010; Murakami et al. 2012).

The new version of the MRI-AGCM—MRI-AGCM3.2—was developed from version 3.1. The differences between the two versions are described in Mizuta

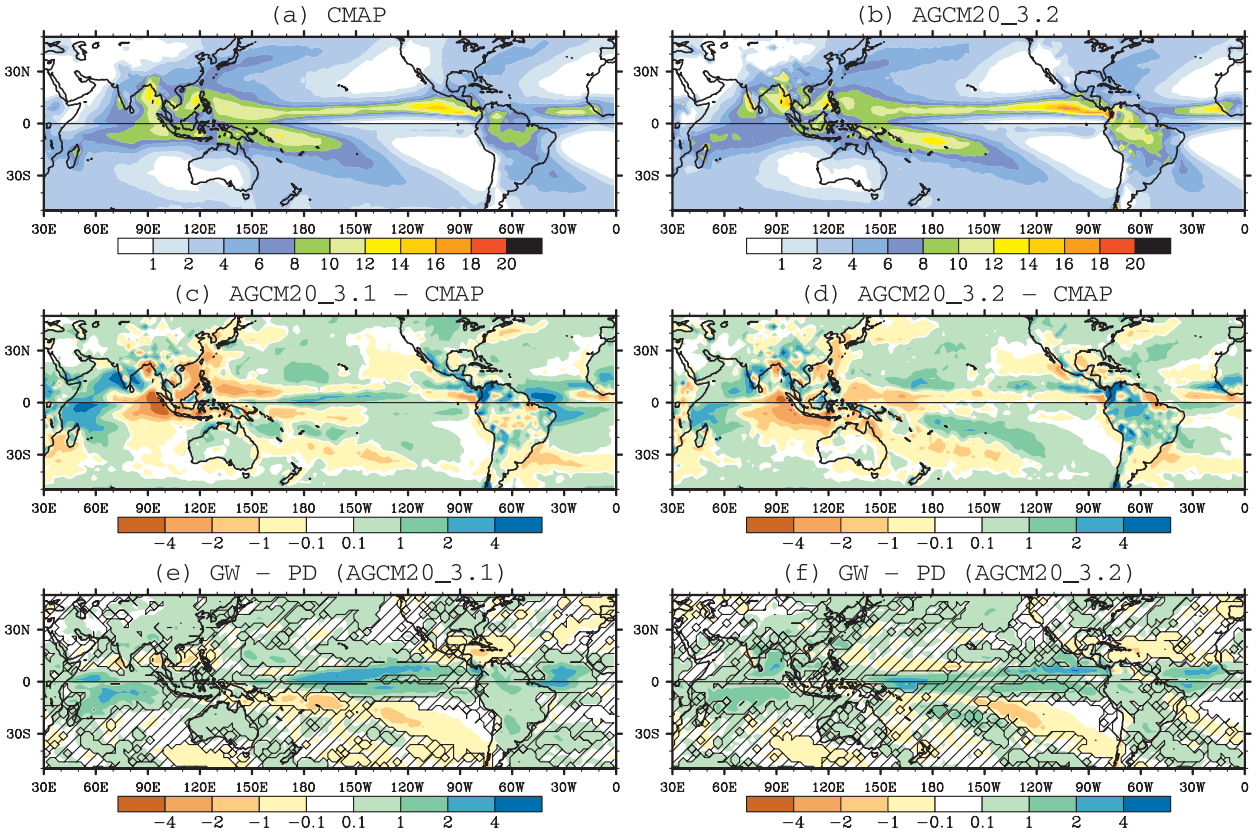

FIG. 1. Climatological mean precipitation (mm day^{-1}) during the peak tropical cyclone season for (a) observations, (b) the 25-yr PD simulation using AGCM20_3.2, (c) the difference between AGCM20_3.1 and observations, (d) the difference between AGCM20_3.2 and observations, (e) the projected future change using AGCM20_3.1, and (f) the projected future change using AGCM20_3.2. Black hatching in (e),(f) indicates that the future change is not statistically significant at the 90% confidence level (two-sided Student's *t* test).

et al. (2012). The dynamical core of version 3.2 uses hydrostatic primitive equations and is solved using a spectral transform method of spherical harmonics, and is unchanged from version 3.1. Four more vertical levels have been added to the model stratosphere. As a result, the arrangement of vertical levels has been changed from 60 levels with the model top at 0.1 hPa in version 3.1 to 64 levels with the model top at 0.01 hPa in version 3.2. Murakami et al. (2011) conducted multiphysics and multi-SST ensemble projections using the 60-km-mesh model version 3.2 to address the relative impacts of differences in projected SST changes and differences in model physics on projected future changes in TC activity at global and regional scales.

Some parameterizations of physical processes have been updated or changed in version 3.2 from version 3.1; the details of these changes are documented in Mizuta et al. (2012). Of particular relevance to this study is the use of a new cumulus convection scheme, which substantially improves the simulation of tropical precipitation and TC climatology. Version 3.1 is equipped with a prognostic Arakawa–Schubert (AS) cumulus convection scheme (Arakawa and Schubert 1974; Randall and Pan 1993). In this scheme, multiple convective updrafts with different heights are explicitly calculated within a single grid cell, with each updraft represented as a simplified entraining plume. A new cumulus scheme, based on the Tiedtke (1989) scheme, has been introduced to version 3.2. In the original Tiedtke scheme, only a single convective updraft is calculated within each grid cell, but this updraft is represented as a more detailed entraining and detraining plume than updrafts in the AS scheme. The new cumulus scheme developed for version 3.2 accounts for multiple detailed entraining and detraining plumes by interpolating two convective updrafts with different rates of turbulent entrainment and detrainment (Yukimoto et al. 2011). Thus, the new cumulus convection scheme combines the advantages of both the AS and the original Tiedtke schemes.

Figures 1a,b show the spatial distributions of climatological mean precipitation during the peak TC seasons in each hemisphere for observations from the Climate

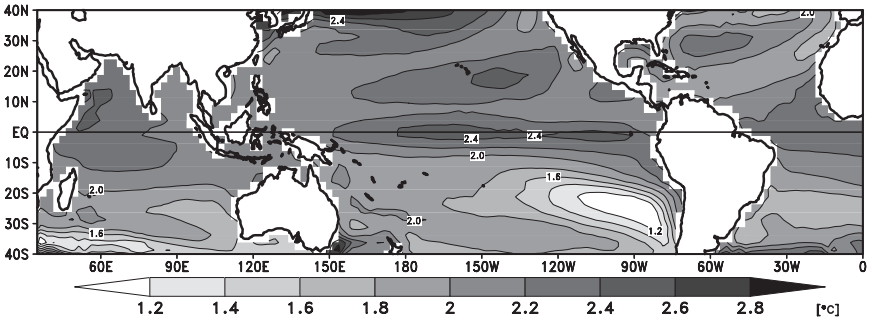

FIG. 2. Annual mean of prescribed future changes in SST (°C).

Prediction Center Merged Analysis of Precipitation (CMAP; Xie and Arkin 1997) and for version 3.2, respectively. The peak TC season in the Northern Hemisphere (NH) is defined as the boreal summer [May–October (MJJASO)], while that in the Southern Hemisphere (SH) is defined as the austral summer [November–April (NDJFMA)]. Figure 1c shows the bias of the climatological mean precipitation simulated in the peak TC seasons by version 3.1 relative to the CMAP observations, while Fig. 1d shows the bias of version 3.2. The amplitude of the biases relative to CMAP observations is generally reduced from version 3.1 to version 3.2. For example, underestimations of precipitation over the Maritime Continent and WNP are less severe in version 3.2 than in version 3.1, so are overestimations of precipitation over the Indian Ocean and tropical Atlantic. Additional comparisons between observations and present-day climate, as simulated by versions 3.1 and 3.2, have been given in Mizuta et al. (2012). In addition to improvements in climatological mean precipitation during the peak TC season, version 3.2 provides more realistic simulations of the seasonal march of the East Asian summer monsoon and blocking highs over the Pacific. The Madden–Julian oscillation (MJO; Madden and Julian 1972, 1994), which is important for TC genesis, is simulated reasonably well by version 3.1, although the amplitude of the simulated MJO is much weaker than that observed (Rajendran et al. 2008; Liu et al. 2009). The amplitude of the MJO simulated by version 3.2 is stronger than that simulated by version 3.1, but it remains weaker than that observed (see Mizuta et al. 2012).

This study considers results from both 20- and 60-km resolutions using versions 3.1 and 3.2. All parameters in the dynamical and physical processes in the 60-km models are exactly same as in the 20-km models. The 20-km-resolution models are herein referred to as AGCM20_3.1 and AGCM20_3.2 for versions 3.1 and 3.2, respectively, and the 60-km-resolution models are referred to as AGCM60_3.1 and AGCM60_3.2, respectively.

b. Simulation settings and observational datasets

The simulation settings and observational datasets are identical to those used in previous studies (Murakami and Sugi 2010; Murakami and Wang 2010; Murakami et al. 2012). A ''time slice'' method (Bengtsson et al. 1996) is applied in this study, in which the high-resolution AGCM is forced by prescribed SSTs as the lower boundary condition. The PD realization is an ''Atmospheric Model Intercomparison Project style'' simulation in which the lower boundary conditions are prescribed as the observed monthly-mean SST and sea ice concentration (SIC) during 1979–2003 of the Met Office Hadley Centre Sea Ice and Sea Surface Temperature version 1 (HadISST1; Rayner et al. 2003). The GW future simulation is a targeted projection of the last quarter of the twenty-first century (2075–99). The monthly-mean lower boundary conditions prescribed for the GW simulation are calculated as a multimodel ensemble mean of SST and SIC from the future projections by the 18 models of the World Climate Research Programme's Coupled Model Intercomparison Project phase 3 (CMIP3) under the Special Report on Emissions Scenarios (SRES) A1B scenario (Solomon et al. 2007). Detrended interannual variations of the observed SST are added to this multimodel ensemble mean [see Mizuta et al. (2008) for the details], with the assumption that interannual variations of SST and SIC in the GW projection are similar to those of the present day. Figure 2 shows the prescribed future changes in the annual mean SST. Note that SST warming is spatially inhomogeneous (Xie et al. 2010): greater warming occurs in the northern tropics than in the southern tropics. The greatest SST warming occurs in the central Pacific (CP), eastern Pacific, and tropical Atlantic.

The TC climatology for the PD simulations is validated using the global TC dataset compiled on the Unisys Corporation website (Unisys 2011). This dataset consists of best-track TC data compiled by the National Hurricane Center (NHC) and Joint Typhoon Warning Center

(JTWC), and contains historical TC information, such as the location, intensity (maximum 1-min surface wind speed), and central sea level pressure (SLP) of the storms at 6-h intervals from 1851 to 2011 (note that the record period is basin dependent). In this study, we consider only TCs of tropical storm intensity or stronger (i.e., TCs that possess 1-min sustained surface wind speeds of 35 kt or greater) between 1979 and 2003.

c. Detection algorithm for tropical cyclones

TCs are detected in the model by using globally uniform criteria for 6-hourly model outputs. These criteria are based on those reported in Oouchi et al. (2006) but with some modifications (Murakami et al. 2011). Some criteria are optimized for a given model configuration to ensure that the present-day global annual mean TC number matches that observed (84 per year for the period 1979–2003). The values listed after each of the following criteria show the model-dependent values used for the optimization (from left, values are for AGCM20_3.1, AGCM20_3.2, AGCM60_3.1, and AGCM60_3.2, respectively):

1) The maximum relative vorticity at 850 hPa exceeds 1.2×10^{-4}, 2.0×10^{-4}, 8.0×10^{-5}, and 8.0×10^{-5} s^{-1}.
2) The maximum wind speed at 850 hPa exceeds 17.0, 17.0, 13.0, and 13.0 m s^{-1}.
3) There is an evident warm core aloft, namely, the sum of the temperature deviations at 300, 500, and 700 hPa exceeds 2.0, 2.0, 1.0, and 0.8 K. The temperature deviation for each level is computed by subtracting the maximum temperature from the mean temperature over the $10° \times 10°$ grid box centered nearest to the location of maximum vorticity at 850 hPa.
4) The maximum wind speed at 850 hPa is greater than the maximum wind speed at 300 hPa.
5) To remove tropical monsoon depressions in the North Indian Ocean (NIO), the radius of maximum mean wind speed must be less than 100, 100, 200, and 200 km from the detected storm center. This condition is applied in the NIO only.
6) The duration of each detected storm must exceed 36 h. When a single TC satisfies all the criteria intermittently, it is considered as multiple TC generation events. To prevent multiple counts of a single TC, a single time step failure is allowed.

Criterion 5 is necessary because we have found that monsoon depressions in the NIO may be detected as TCs during the monsoon season regardless of the other detection criteria. This is because monsoon depressions have some characteristics in common with TCs (Murakami et al. 2011). The monsoon depression in the north Indian Ocean is a cyclonic low pressure system that forms within the monsoon trough during the monsoon season, characterized by 1) a large horizontal scale of 2000−3000 km, 2) maximum wind speeds located at more than 200 km from the center of the system, and 3) a deep vertical structure that extends up to 8 km (Ding and Sikka 2006). The effects of strong wind shear prevent a monsoon depression from developing into a TC during the monsoon season. We could distinguish TCs from monsoon depressions by criterion 5; however, the use of another criterion, such as vertical wind shear, may enable the distinction between monsoon depressions and TCs as well.

It is possible that the present results are dependent on the selected TC detection algorism. In addition, when different models are compared, model-dependent criteria may affect the results, implying that it is impossible to access the relative performance of the models. We performed a preliminary investigation of dependency of selected TC detection algorism on global TC distribution and future changes in the TC genesis number using the resolution-dependent criteria proposed by Walsh et al. (2007). The results support the robustness of our present findings documented in this study: version 3.2 yields improved global TC distributions compared with version 3.1 (as shown in section 3a) and fractional future changes in the TC genesis number (as shown in section 4a) are robust among the various TC detection algorisms.

TC positions are counted for each $2.5° \times 2.5°$ grid box within the global domain at 6-h intervals. The total count for each grid box is defined as the TC frequency (TCF). The first detected position is defined as the location of TC genesis, and the TGF at each grid box is counted similarly to TCF. Because the computed frequency fields are noisy, they are smoothed using a 9-point average weighted by distance from the center of the grid box. Most TCs are generated during the peak seasons of the boreal summer (MJJASO) for the Northern Hemisphere and the austral summer (NDJFMA) for the Southern Hemisphere. This study therefore focuses primarily on TC changes during the corresponding peak TC season.

Nine ocean basins are considered in our analysis: global (GL), NH, SH, NIO, WNP, eastern North Pacific (ENP), NAT, south Indian Ocean (SIO), and South Pacific Ocean (SPO) (see Fig. 3 for regional boundaries).

3. Evaluation of the present-day simulation

a. TC tracks, TC number, and TC frequency of occurrence

Figure 3 compares the observed and simulated distributions of TC tracks during all seasons (not only the

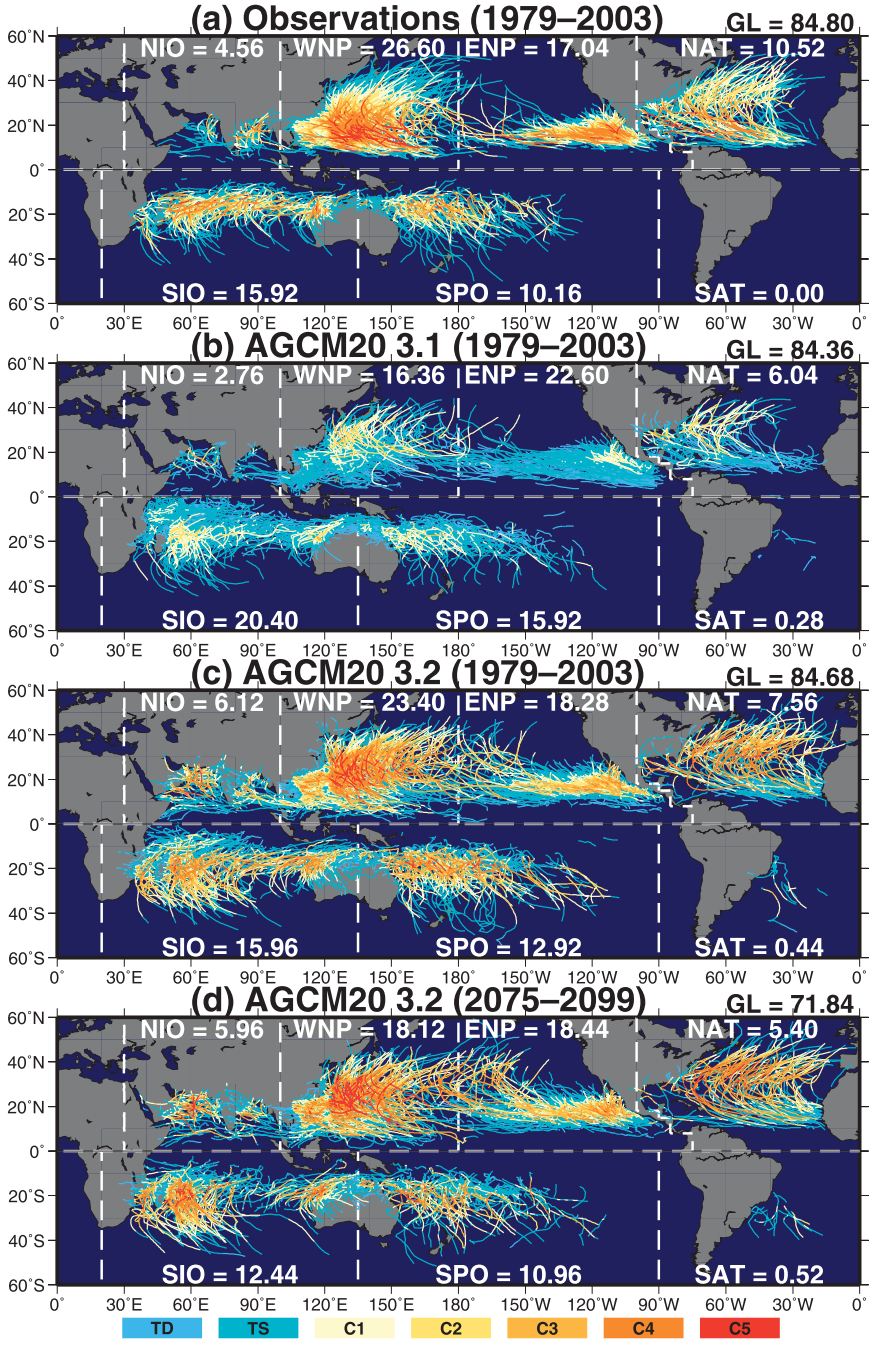

FIG. 3. Global distribution of TC tracks during all seasons from 1979 to 2003 for (a) observations, (b) the PD simulation using AGCM20_3.1, (c) the PD simulation using AGCM20_3.2, and (d) the GW projection using AGCM20_3.2. The numbers for each basin show the annual mean number of TCs. TC tracks are colored according to the intensities of the TCs as categorized by the Saffir–Simpson hurricane wind scale [e.g., tropical depression (TD), tropical storms (TSs), and C1–C5].

peak TC seasons), and the annual mean TC numbers are listed in Table 1. Compared with observations, the AGCM20_3.1 PD simulation (Fig. 3b and Table 1b) underestimates the TC number in the WNP by about 40% and simulates an unrealistically large proportion of TCs in the SH. These biases are substantially reduced in the AGCM20_3.2 PD simulation (Fig. 3c and Table 1c). Similar improvements occur in the simulation using AGCM60_3.2 (Table 1e) relative to that using AGCM60_3.1 (Table 1d).

TABLE 1. Annual mean TC numbers in each ocean basin for (a) observations, (b) AGCM20_3.1, (c) AGCM20_3.2, (d) AGCM60_3.1, and (e) AGCM60_3.2. Shown is the annual mean TC number according to the PD simulation and the GW projection, projected future changes in the annual mean TC number (%), and the level of statistical significance (SIG) of the projected change (%) (two-sided Student's *t* test). Statistically significant changes are highlighted in bold.

(a) Observations	GL	NH	SH	NIO	WNP	ENP	NAT	SIO	SPO
	84.8	58.7	26.1	4.6	26.6	17.0	10.5	15.9	10.2
(b) AGCM20_3.1	GL	NH	SH	NIO	WNP	ENP	NAT	SIO	SPO
PD	84.4	47.8	36.6	2.8	16.4	22.6	6.0	20.4	15.9
GW	65.4	38.1	27.4	2.4	11.9	17.3	6.5	18.3	8.8
GW − PD	**−22.5**	**−20.3**	**−25.1**	−14.3	**−27.4**	**−23.5**	+8.3	−10.3	**−44.7**
SIG	**99**	**99**	**99**	—	**99**	**99**	—	—	**99**
(c) AGCM20_3.2	GL	NH	SH	NIO	WNP	ENP	NAT	SIO	SPO
PD	84.7	55.4	29.3	6.1	23.4	18.3	7.6	16.0	12.9
GW	71.8	47.9	23.9	6.0	18.1	18.4	5.4	12.4	11.0
GW − PD	**−15.2**	**−13.5**	**−18.4**	−1.6	**−22.6**	+0.5	**−28.9**	**−22.5**	−14.7
SIG	**99**	**99**	**99**	—	**99**	—	**99**	**95**	—
(d) AGCM60_3.1	GL	NH	SH	NIO	WNP	ENP	NAT	SIO	SPO
PD	83.8	54.1	29.7	2.8	12.1	33.0	6.1	18.2	11.2
GW	64.2	41.6	22.6	3.4	9.7	22.5	6.0	15.5	6.8
GW − PD	**−23.4**	**−23.1**	**−23.9**	+21.4	−19.8	**−31.8**	−1.6	**−14.8**	**−39.3**
SIG	**99**	**99**	**99**	—	—	**99**	—	**90**	**99**
(e) AGCM60_3.2	GL	NH	SH	NIO	WNP	ENP	NAT	SIO	SPO
PD	83.5	55.0	28.5	5.9	29.8	13.4	5.9	16.4	11.7
GW	63.6	42.2	21.4	5.1	21.4	12.1	3.6	12.4	8.6
GW − PD	**−23.8**	**−23.3**	**−24.9**	−13.6	**−28.2**	−9.7	**−39.0**	**−24.4**	**−26.5**
SIG	**99**	**99**	**99**	—	**99**	—	**99**	**95**	**99**

Table 2 presents the root-mean-square error (RMSE) and Taylor skill score I for the simulated spatial distributions of TCF during the peak TC season for each basin, as calculated against the observed distribution. The Taylor skill score I, which is a combination of the spatial variance and spatial correlation, ranges from 0.0 (no skill) to 1.0 (perfect skill) (Taylor 2001). The scores for both AGCM20 and AGCM60 are improved from version 3.1 to version 3.2 in the WNP, SIO, and SPO but are comparable or worse in the NIO, ENP, and NAT. The simulated TCF in the WNP, which was severely underestimated in version 3.1, is substantially improved in version 3.2. The scores for the AGCM20 simulations are also generally higher than those for the AGCM60 simulations, consistent with the hypothesis that a higher-resolution model yields a better TC climatology (see also Murakami and Sugi 2010). The improvements in TGF are similar to those in TCF (not shown), although AGCM20_3.2 overestimates TGF over the NIO and underestimates both TGF and TCF over the Caribbean Sea and Gulf of Mexico.

The improved simulation of the global distributions of TCs in AGCM20_3.2 appears to be due to differences in large-scale climatological fields. We have examined a number of dynamical (relative vorticity at 850 hPa, omega at 500 hPa, vertical wind shear between 200 and 850 hPa, and synoptic-scale disturbances) and thermodynamic [relative humidity at 700 hPa and maximum potential intensity (MPI) defined by Emanuel (1995) and Bister and Emanuel (1998)] mean fields (Fig. 4) that are relevant to the improvement in the simulated TGF (Murakami et al. 2011). Because TC existence may affect the climatological monthly-mean fields in regions where TCF is high, grid cells with values of TCF greater

TABLE 2. RMSE and Taylor skill score I (parentheses) of the simulated climatological mean spatial distribution of TCF during the peak TC season relative to observations. Scores are computed a region between 40°N and 40°S for each ocean basin.

	AGCM20_3.1	AGCM20_3.2	AGCM60_3.1	AGCM60_3.2
GL	0.40 (0.92)	0.33 (0.95)	0.44 (0.85)	0.40 (0.85)
NH	0.40 (0.92)	0.36 (0.96)	0.54 (0.76)	0.51 (0.81)
SH	0.40 (0.77)	0.29 (0.91)	0.30 (0.89)	0.22 (0.93)
NIO	0.11 (0.84)	0.29 (0.42)	0.11 (0.52)	0.15 (0.71)
WNP	0.74 (0.70)	0.33 (0.97)	0.94 (0.52)	0.41 (0.96)
ENP	0.31 (0.98)	0.55 (0.95)	0.55 (0.90)	0.90 (0.41)
NAT	0.21 (0.87)	0.27 (0.83)	0.28 (0.71)	0.31 (0.62)
SIO	0.56 (0.79)	0.40 (0.92)	0.50 (0.85)	0.33 (0.90)
SPO	0.41 (0.67)	0.30 (0.84)	0.17 (0.96)	0.19 (0.94)

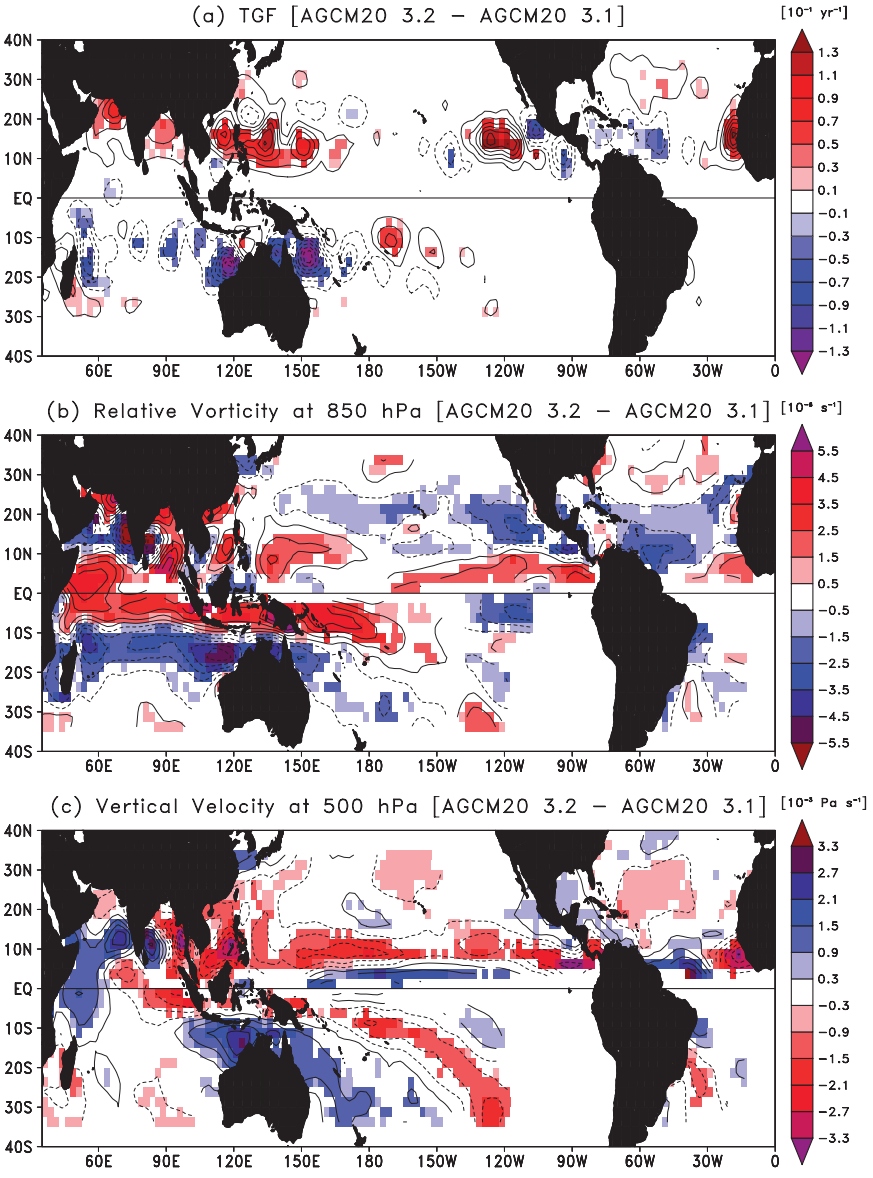

FIG. 4. Differences between PD simulations by AGCM20_3.2 and AGCM20_3.1 in terms of (a) TGF (10^{-1} yr^{-1}), (b) relative vorticity at 850 hPa (10^{-6} s^{-1}) (sign is reversed in the SH so that positive values indicate cyclonic anomaly), and (c) vertical p velocity at 500 hPa (10^{-3} Pa s^{-1}) during the peak TC season. Solid contours indicate positive values, and dashed contours indicate negative values. Shaded areas indicate that differences are significant to at least the 90% confidence level (two-sided Student's t test).

than 3.0 have been removed from monthly-mean data prior to the calculation of the climatological monthly mean (Murakami et al. 2011).

Among the analyzed fields, the changes in relative vorticity at 850 hPa (Fig. 4b) are the most closely correlated to those of TGF (Fig. 4a), which is evaluated in terms of spatial correlation coefficients. In particular, the monsoon trough in the WNP during the boreal summer is deeper in AGCM20_3.2 than in AGCM20_3.1, resulting in greater positive vorticity in the WNP basin. This increase in vorticity is related to the increase in convective activity over the WNP in AGCM20_3.2 (Fig. 1). Mizuta et al. (2012) reported that, when compared with AGCM20_3.1, AGCM20_3.2 simulates a larger westerly moisture flux over the NIO and a larger southwesterly moisture flux over the East China Sea, resulting in a larger westerly moisture flux over the Philippine Sea. The resultant moisture supply to the WNP creates a favorable thermodynamic environment for convective activity in the WNP. Active convection in the WNP

TABLE 3. Correlation coefficients between the observed and simulated interannual variability of tropical cyclone genesis number for each basin. Correlation coefficients between the observed and simulated climatological monthly seasonal cycle of TC genesis number are given in parentheses. Bold number indicates that the correlation coefficient is statistically significant at the 95% level (Pearson's product-moment correlation significance test).

	(a) AGCM 20_3.1	(b) AGCM 20_3.2	(c) AGCM 60_3.1	(d) AGCM 60_3.2
GL	**0.48 (0.62)**	**0.53 (0.91)**	0.31 (**0.63**)	0.27 (**0.87**)
NH	**0.48 (0.89)**	0.37 (**0.99**)	0.33 (**0.84**)	0.37 (**0.98**)
SH	**0.70 (0.99)**	**0.62 (0.97)**	**0.43 (0.99)**	0.32 (**0.98**)
NIO	0.08 (**0.88**)	**0.49 (0.65)**	−0.03 (**0.80**)	−0.22 (**0.79**)
WNP	**0.52 (0.90)**	**0.53 (0.97)**	0.38 (**0.88**)	**0.47 (0.93)**
ENP	−0.24 (**0.63**)	0.16 (**0.98**)	−0.19 (0.47)	0.15 (**0.95**)
NAT	**0.44 (0.98)**	**0.46 (0.97)**	**0.54 (0.99)**	**0.51 (0.93)**
SIO	**0.77 (0.92)**	**0.64 (0.92)**	**0.42 (0.95)**	**0.47 (0.95)**
SPO	0.09 (**0.99**)	0.37 (**0.98**)	0.20 (**0.97**)	0.09 (**0.99**)

induces positive vorticity and enhances surface moisture convergence, creating a positive feedback (Mizuta et al. 2012). This positive feedback appears to enhance the realism of the simulated dynamical and thermodynamic environments in the WNP and results in an improved TC climatology.

The next most closely related factor is the changes in vertical velocity at 500 hPa (Fig. 4c). This relationship is consistent with the improvements in the climatological distribution of precipitation (Fig. 1) that are attributed to the new convection scheme used in version 3.2. AGCM20_3.1 overestimates TGF in the SH (Fig. 3b). This bias has been eliminated in AGCM20_3.2 by reducing the climatological upward motion (Fig. 4c) and cyclonic vorticity (Fig. 4b) in the TC genesis basins. As mentioned in section 2a, the simulation of the MJO amplitude in version 3.2 is improved compared to that in version 3.1; however, it is unlikely to be a major factor because AGCM20_3.2 continues to underestimate the MJO amplitude compared to observations. Improvements in the simulation of the tropical synoptic-scale disturbances (TSDs) (Lau and Lau 1990), defined as the variance of 2–8-day bandpass-filtered 850-hPa vorticity, could also explain the improvements in the simulated TGF in version 3.2; however, no significant differences in the simulation of synoptic disturbances are found among the models (not shown).

b. *Interannual and seasonal variations of TC genesis number*

Table 3 presents correlation coefficients between the simulated and the observed interannual variation of TC genesis number for each basin. Although AGCM20_3.2 (Table 3b) shows higher correlation coefficients than the other model versions in some ocean basins, these differences are not statistically significant. All the models show similar significant correlations with observations in the WNP, NAT, and SIO, indicating that the models have similar skills in reproducing the year-to-year variations of TC genesis in these basins. The correlation coefficients in the NAT (about 0.45–0.55) are low compared with other global modeling studies, such as 0.83 reported by Zhao et al. (2009) and 0.78 reported by LaRow et al. (2008), although the high correlations reported in these studies were obtained from ensemble simulations.

The parentheses in Table 3 show correlation coefficients between the simulated and the observed seasonal cycles of the TC genesis number. The seasonal cycle of the TC genesis number simulated by version 3.2 is substantially improved in WNP and ENP relative to that simulated by version 3.1, but it is worse in NIO, where version 3.2 overestimates the TC genesis number during the peak TC season.

c. *TC intensity*

Earlier studies have reported that AGCM20_3.1 underestimates TC intensity (Oouchi et al. 2006; Murakami et al. 2008; Murakami and Sugi 2010). Figure 3b shows the distribution of TC intensities simulated by AGCM20_3.1, and Table 4b lists the mean TC intensity simulated by AGCM20_3.1. These simulated intensities are much weaker than those observed. Figure 3c and Table 4c show the distribution of TC intensities and mean TC intensity simulated by AGCM20_3.2, which are much more intense than those simulated by AGCM20_3.1. AGCM20_3.2 reproduces category 4 and 5 (C4 and C5, respectively) TCs more realistically than AGCM20_3.1. The difference in TC intensity between these two versions stems from the differences in the cumulus convection scheme. Figure 5 compares snapshots of two 48-h simulations of a TC using AGCM20_3.2 for which the same initial conditions are prescribed. The prescribed initial conditions describe a developing vortex that has not yet reached TC intensity. The sole difference between these two simulations is the cumulus convection scheme, so that the differences between the model results illustrate sensitivity to the convection scheme. The minimum SLP of the TC simulated using the AS convection scheme is 992 hPa (Fig. 5a), while that simulated using the new convection scheme is 975 hPa (Fig. 5b). In the simulation with the AS convection scheme, precipitation within the eyewall region and inner core (the region within 200 km of the TC center) is weak, and precipitation outside the eyewall region is broadly distributed. In the simulation with the new convection scheme, precipitation is intense within the eyewall region and precipitation outside the eyewall region is locally concentrated in spiral rainbands.

TABLE 4. Mean maximum surface wind speed (m s^{-1}) of TCs in each basin for (a) observations and projection results by (b) AGCM20_3.1 and (c) AGCM20_3.2. For the projections, also shown are the mean of the PD experiment, mean of the future GW experiment, future changes [fractional change (%) in parenthesis], and the SIG (Welch's *t* test) of the future changes. Also shown are the values for the lifetime maximum surface wind speed (m s^{-1}) (d-f).

		(b) AGCM20_3.1				(c) AGCM20_3.2			
Mean	(a) Observations	PD	GW	GW − PD	SIG (%)	PD	GW	GW − PD	SIG (%)
GL	32.4	20.9	23.3	+2.3 (+11.2)	99	30.6	31.9	+1.2 (+4.0)	99
NH	33.2	20.7	23.2	+2.5 (+12.2)	99	30.6	32.4	+1.7 (+5.7)	99
SH	30.4	21.2	23.3	+2.1 (+10.0)	99	30.6	30.8	+0.1 (+0.4)	—
NIO	27.0	21.3	22.3	+1.0 (+4.7)	99	28.8	30.8	+1.9 (+6.6)	99
WNP	34.6	21.6	25.5	+3.9 (+18.1)	99	32.9	35.3	+2.3 (+7.1)	99
ENP	32.2	19.1	21.3	+2.2 (+11.7)	99	26.7	28.3	+1.6 (+6.1)	99
NAT	32.3	23.2	24.3	+1.1 (+4.9)	99	33.6	37.0	+3.4 (+10.0)	99
SIO	30.6	21.8	23.9	+2.1 (+9.6)	99	30.0	32.1	+2.1 (+6.9)	99
SPO	30.0	20.2	21.8	+1.6 (+8.0)	99	31.6	28.6	−3.0 (−9.6)	99
Lifetime		(e) AGCM20_3.1				(f) AGCM20_3.2			
max	(d) Observations	PD	GW	GW − PD	SIG (%)	PD	GW	GW − PD	SIG (%)
GL	38.8	23.9	27.0	+3.1 (+12.9)	99	40.0	41.1	+1.2 (+2.9)	95
NH	39.7	23.6	26.5	+2.9 (+12.1)	99	40.1	42.0	+1.9 (+4.6)	99
SH	36.7	24.3	27.7	+3.4 (+14.1)	99	39.7	39.5	−0.3 (−0.7)	—
NIO	31.1	24.9	27.0	+2.1 (+8.3)	—	38.2	40.3	+2.0 (+5.3)	—
WNP	42.8	25.5	29.5	+4.0 (+15.5)	99	45.1	47.9	+2.8 (+6.2)	95
ENP	38.5	21.3	24.0	+2.7 (+12.8)	99	33.8	35.8	+2.0 (+5.9)	95
NAT	37.8	26.6	27.2	+0.6 (+2.4)	—	40.3	44.0	+3.7 (+9.3)	90
SIO	37.1	25.6	29.5	+3.9 (+15.2)	99	39.8	42.6	+2.8 (+7.1)	95
SPO	36.0	22.6	24.3	+1.7 (+7.4)	90	39.9	35.9	−4.0 (−10.1)	99

Figures 5c,d also show the simulated convective and large-scale heating rates from the simulation with the AS convective scheme (Fig. 5c) and from that with the new convective scheme (Fig. 5d). In the simulation with the AS scheme, convective heating is dominant and the level of maximum heating occurs at approximately 400 hPa, indicating that the AS scheme preferably generates deep convective updrafts. Although the new convection scheme produces a smaller convective heating rate at upper levels, large-scale condensation contributes considerably to the heating rate at the upper levels (as well as total column heating). Convective heating is more tightly constrained in the new scheme, which appears to induce intense grid-scale upward motions and promote large-scale condensation, resulting in the development of a more intense TC. The intensification of grid-scale upward motion enhances the moisture supply at low levels, which further intensifies the TC. This positive feedback in the new convective scheme appears to contribute to more intense TCs than the simulation with the AS convective scheme. Figures 6a–c compare composite TC structure between AGCM20_3.1 and AGCM20_3.2 simulated for the PD simulations. Composite structures are made for the TCs at their lifetime maximum intensity in the NH. AGCM20_3.2 simulates smaller minimum SLP, and more intense wind speed and precipitation than AGCM20_3.1. Both versions show that the maximum tangential wind speed is located less than 100 km from the storm center (Fig. 6c), which is consistent with observations (Frank 1984; Murakami et al. 2008). Although the available observed mean 3D TC structure is limited for comparison, AGCM20_3.2 shows reasonable 3D structures (Figs. 6d–f) as follows: a maximum in tangential wind speed at approximately 850 hPa (Fig. 6a), an anticyclonic circulation in the upper troposphere (Fig. 6d), an inflow boundary layer (Fig. 6e; Frank 1984); and a warm core in the upper–middle troposphere at 300 hPa (Fig. 6f; Hawkins and Rubsam 1968). Figure 7 shows the relationship between the maximum surface wind speed and the minimum SLP for all TCs. Also shown in the figure is Atkinson and Holiday's (1977) nonlinear regression curve derived from observations in the WNP (pink dashed curve). Both the AGCM20_3.1 (blue dots in Fig. 7a) and AGCM20_3.2 (blue dots in Fig. 7b) simulations capture well the observed relationship.

Figure 8 compares the two versions in terms of the annual mean frequency of TCs as a function of maximum surface wind speed and compares the annual mean number of TCs as a function of the lifetime maximum surface wind speed. The intensities of TCs identified in the AGCM20_3.1 PD simulation (blue lines in Figs. 8a–f) are substantially underestimated compared with observations (green lines). The AGCM20_3.1 even simulates weaker TCs than do some models with lower spatial

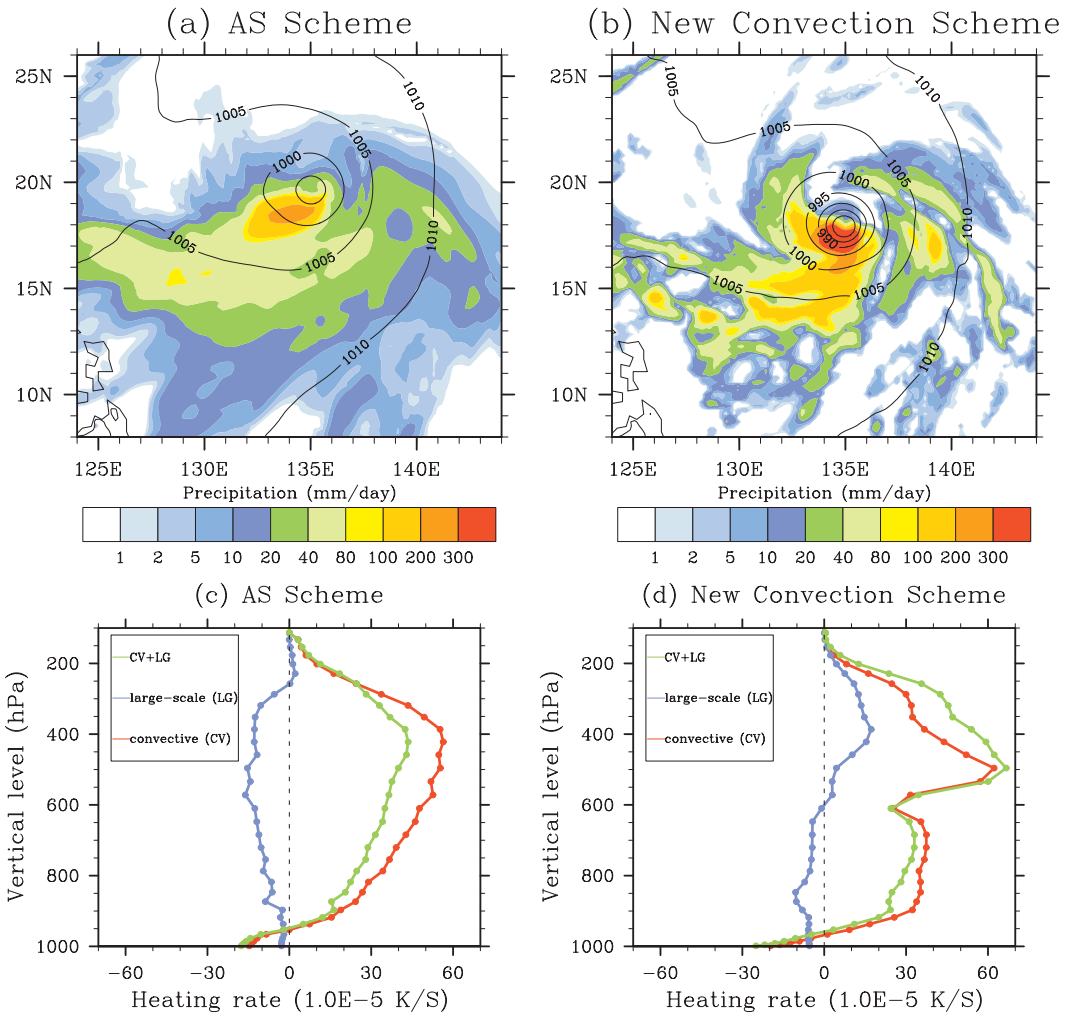

FIG. 5. (a),(b) Snapshots of 48-h simulations initialized under the same initial conditions generated using (a) the AS convection scheme and (b) the new convection scheme. Colors indicate 1-h mean precipitation (mm day^{-1}), and contours indicate instantaneous SLP (hPa). (c),(d) Simulated 1-h mean vertical structure of area mean heating rates (K s^{-1}) in the eyewall region (within 200 km of the storm center) for (c) the AS scheme and (d) the new convection scheme. Blue, red, and green lines indicate heating rates by large-scale condensation, convection, and total (large scale condensation plus convection), respectively.

resolutions [e.g., Fig. 6 in Zhao et al. (2009), in which a 50-km-resolution AGCM was used]. The intensities of the simulated TCs are substantially improved in AGCM20_3.2 (blue lines in Figs. 8g–l), as the annual mean number and frequency of the simulated TCs in each intensity bin are consistent with observations, although version 3.2 overestimates the frequency of strong TCs compared with observations.

4. Projected future changes

a. TC genesis number

Table 1 lists the observed and the projected annual mean TC numbers for each basin. The global and hemispheric TC numbers are significantly reduced in all GW projections, with reductions ranging from 13% to 25%. The projected decrease is larger in the SH than in the NH for all the models. The degree of the projected reduction is smaller in AGCM20_3.2 than in the other models. The differences between AGCM20_3.1 and AGCM60_3.1 appear to be small, so do the differences between AGCM20_3.2 and AGCM60_3.2. Although all the models tend to show significant decreases in the number of simulated TCs in the WNP, SIO, and SPO, the relative changes at the basin scale differ among the models. For example, neither of the simulations using version 3.1 projects significant changes in the number of TCs in the NAT, while both simulations using version

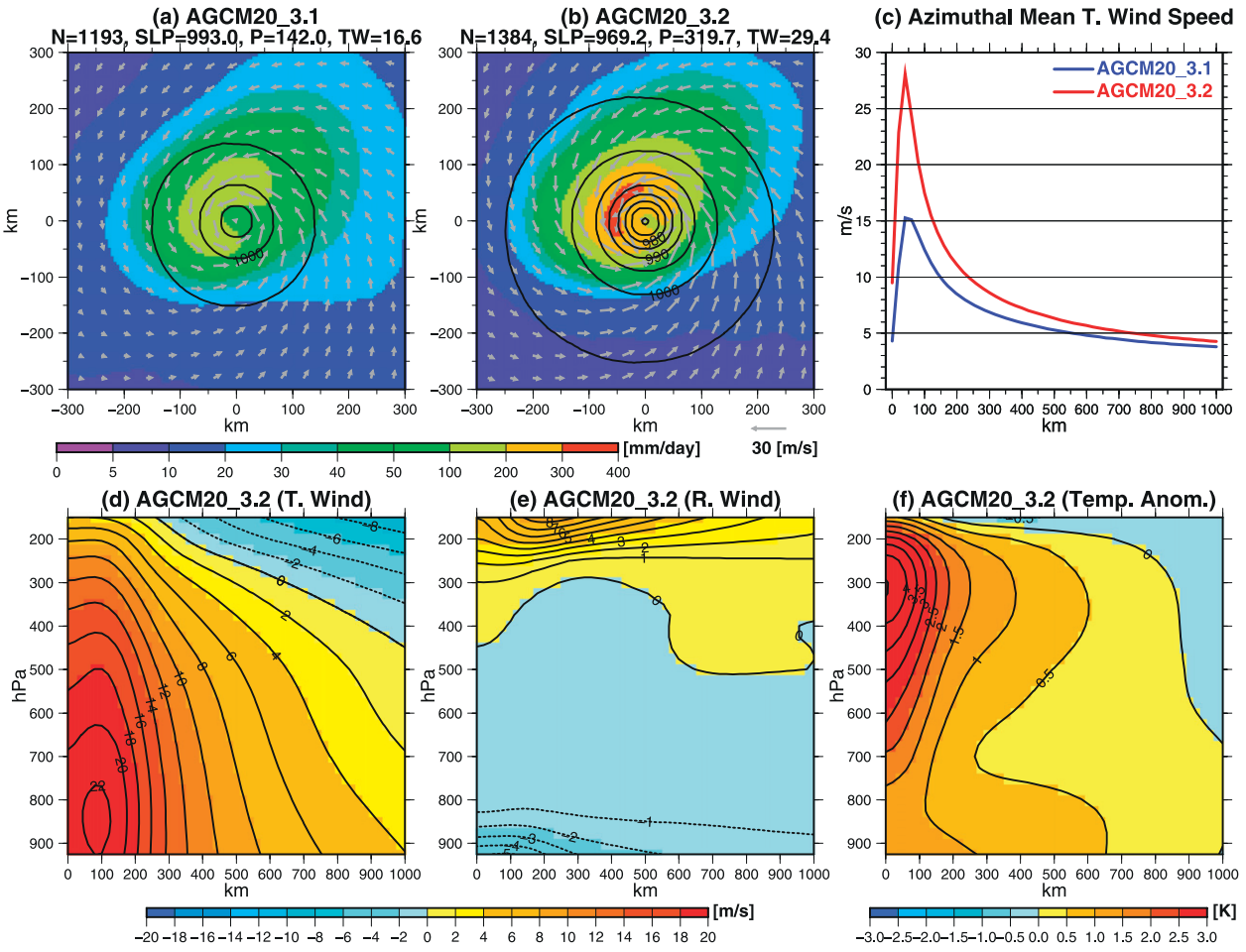

FIG. 6. Composite structure for TCs at their lifetime maximum intensity in the NH. Mean 10-m surface wind speed (m s^{-1}, vectors), precipitation (mm day^{-1}, shading), and SLP (hPa, contours) for PD simulations by (a) AGCM20_3.1 and (b) AGCM20_3.2. The sample size (N), minimum SLP, maximum precipitation (P), and maximum tangential wind speed (TW) are listed in each panel. (c) Azimuthal mean TW (m s^{-1}) for AGCM20_3.1 (blue) and AGCM20_3.2 (red) as a function of distance from the storm center (km). (d)–(f) Composite vertical sections for (d) TW (m s^{-1}, positive values indicate cyclonic flows), (e) radial wind speed (m s^{-1}, positive values indicate inflow), and (f) temperature anomaly (K) (departure from the averaged value within a 2000-km radius), as simulated for the PD by AGCM20_3.2.

3.2 project significant decreases in the NAT. Conversely, both simulations using version 3.1 project significant decreases in the number of TCs in the ENP, while neither of the simulations using version 3.2 projects a significant change.

The results of this study are generally consistent with the range of projected changes reported in previous studies. For example, in their summary of recent modeling studies, Knutson et al. (2010a) reported that the global mean TC frequency is projected to decrease by between 6% and 34% by the end of the twenty-first century, and that the number of TCs in the SH is projected to decrease by a greater fraction than the number of TCs in the NH. Although the AGCM20_3.1 GW simulation projected an increase in the number of TCs in the NAT, most previous models have projected a decrease as climate warms [e.g., supplemental table S1 in Knutson et al. (2010a)]. Moreover, experiments conducted in Knutson et al. (2010a), which projected an increase in TC frequency in the NAT, were based on experiments using MRI models or using the prescribed future SST projected by the coupled MRI model. Overall, the reductions in global and hemispheric TC numbers are robust and independent of model physics, while basin-scale changes in the TC numbers are variable and appear to be dependent on model physics or the spatial pattern of future changes in SST (Murakami et al. 2011).

b. *TC frequency of occurrence*

Figures 9a,b show the spatial distribution of the projected future changes in TCF during the peak TC season from the version 3.1 and version 3.2 ensembles, respectively.

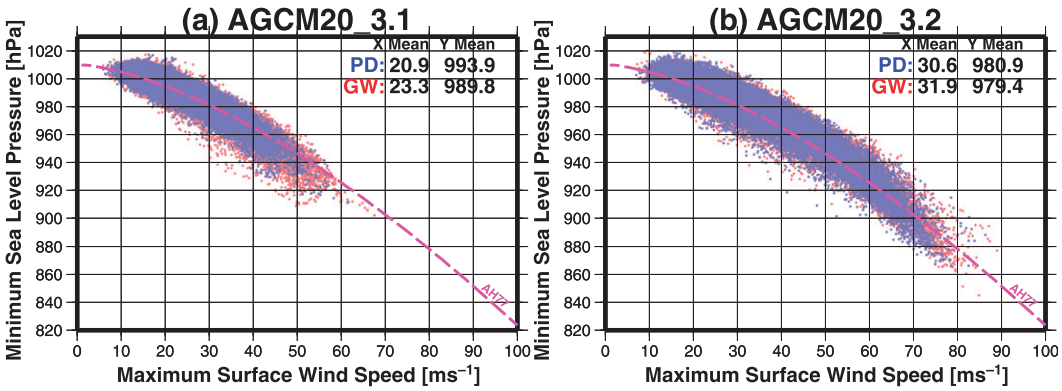

FIG. 7. Maximum surface wind speed (m s^{-1}) vs minimum SLP (hPa) for TCs simulated using (a) AGCM20_3.1 and (b) AGCM20_3.2. Blue dots are data from the PD simulation, and the red dots are from the GW projection. The pink curve is the observationally based regression line proposed by Atkinson and Holiday (1977), based on observed data. Also shown are the mean maximum surface wind speed and the minimum SLP for the PD and GW simulations.

Both versions show similar changes in TCF in the SH, in the western portion of the WNP, and in the central Pacific. However, the projected TCF changes in version 3.1 and version 3.2 differ in the southeastern quadrant of the WNP. Murakami et al. (2012) reported that AGCM20_3.1 projects a significant increase in TCF in the southeastern WNP. Yokoi and Takayabu (2009) also reported similar projected changes over the WNP using five CMIP3 models; however, the projected southeastward shift reported in the two studies is not specific to version 3.2. In contrast, the simulations with version 3.2 project a significant decrease in TCF throughout the entire WNP, which is qualitatively similar to the results reported by Li et al. (2010), who performed a similar analysis using the ECHAM5 global model with 40-km resolution and using the Geophysical Fluid Dynamics Laboratory (GFDL) global model with 50-km resolution. The version 3.1 and version 3.2 models also project different changes in TCF in the NAT. As reported by Murakami and Wang (2010), version 3.1 projects a significant eastward shift of TCF in the NAT in a warmed climate, while version 3.2 projects a decrease in TCF across the entire NAT. It is important to note, however, that the bias in the PD simulation of TCF in the NAT is larger in version 3.2 than in version 3.1 (Table 2). A slight poleward shift in TC tracks is apparent in version 3.1 (Fig. 9a), whereas such a shift is not evident in version 3.2 (Fig. 9b), although poleward shifts in TCF and TGF are clear in AGCM60_3.2 (see Fig. 5 in Murakami et al. 2011).

Figures 9c,d show differences in the projected changes in TCF due to differences in model resolution. These differences are small in general, indicating that the projected future changes in TCF are largely independent of model resolution. This relative insensitivity of the projected changes in TCF to resolution is consistent with the results reported by Murakami and Sugi (2010). This result suggests that ensemble simulations using a lower-resolution version of the AGCM, as demonstrated by Murakami et al. (2011), may be used to evaluate uncertainties in the projected future changes in TCF, given the fact that ensemble climate simulations using the AGCM at 20-km resolution remain computationally expensive.

Model biases must be taken into account when evaluating the projected future climate changes. This is largely because significant decreases (increases) in TCF are difficult to detect for grid cells in which TCF is underestimated (overestimated) in the PD simulation. Model biases in the PD simulations could thus be inherited to the projections of future change. Although there are different ways to calculate the ensemble mean, we propose the following simple weighting method:

$$w_i = \frac{T_i}{R_i} \Big/ \sum_{i=1}^{n} \frac{T_i}{R_i}, \tag{1}$$

where w is the weighting function for each ocean basin, the subscript i refers to the model, n is the number of models included in the ensemble, T is the Taylor skill score I, and R is the RMSE (Table 2). Using this weighting method, simulations from AGCM20_3.1, AGCM20_3.2, AGCM60_3.1, and AGCM60_3.2 contribute 14%, 43%, 8%, and 35%, respectively, to the ensemble mean in the WNP. Figure 9f shows the spatial distribution of the projected changes in TCF according to this weighted ensemble mean. Although the projected future changes calculated in this way differ somewhat from the equally weighted ensemble mean (Fig. 9e), the spatial distributions are qualitatively very similar.

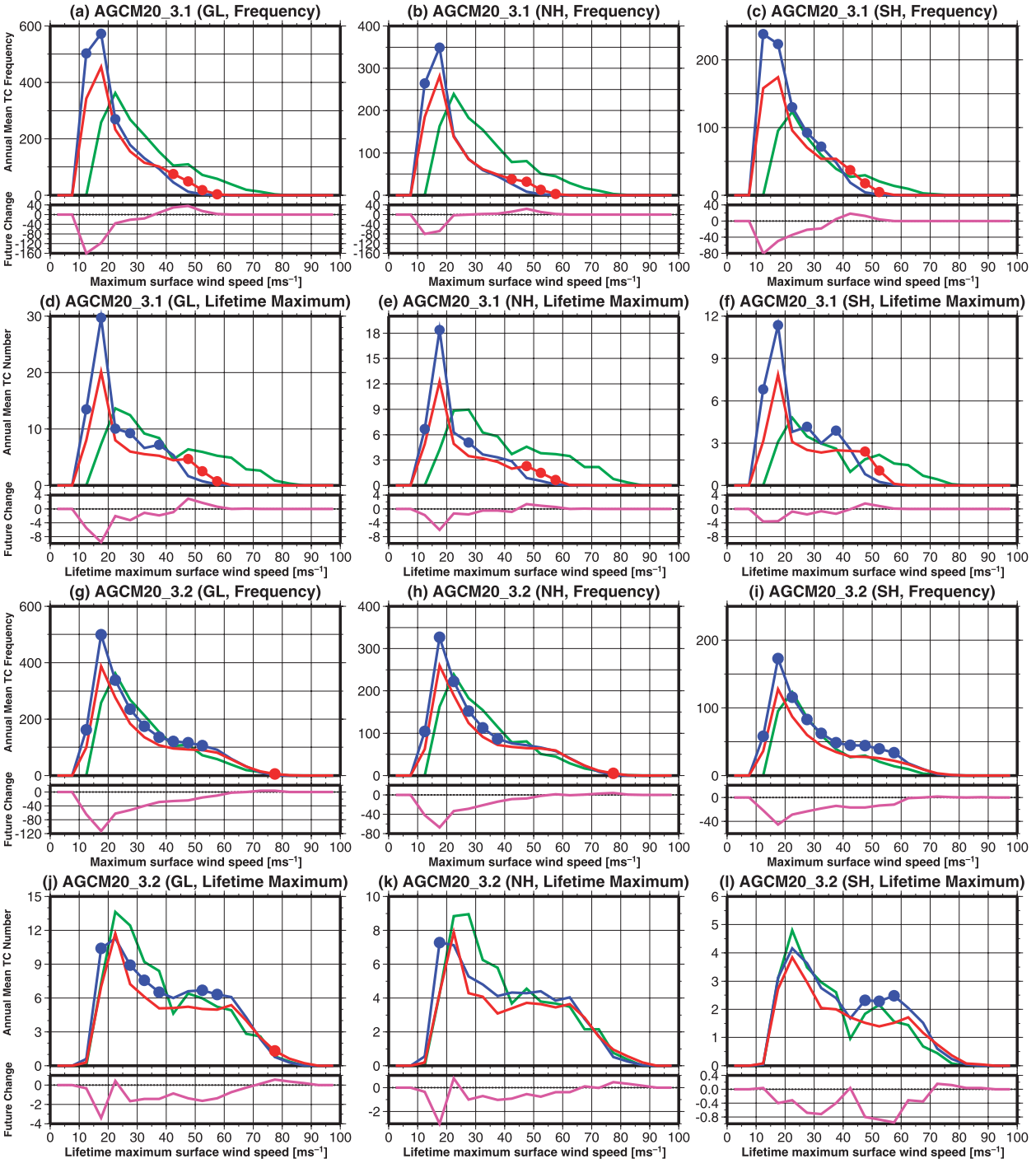

FIG. 8. Annual mean TCF for all TC data, according to observations (1979–2003, green lines), PD simulations (1979–2003, blue lines), and future projections (2075–99, red lines) for the (a) GL, (b) NH, and (c) SH projected using AGCM20_3.1. (d)–(f) As in (a)–(c), but for annual mean TC number for the lifetime maximum surface wind speed (m s^{-1}). (g)–(l) As in (a)–(f), but for AGCM20_3.2. Red (blue) circles indicate that the binned value for the future projection is significantly higher (lower) than that for the PD simulation at the 95% confidence level (two-sided Student's *t* test). Bin width is 5 m s^{-1}. Pink lines show the difference between the future projection and the PD simulation.

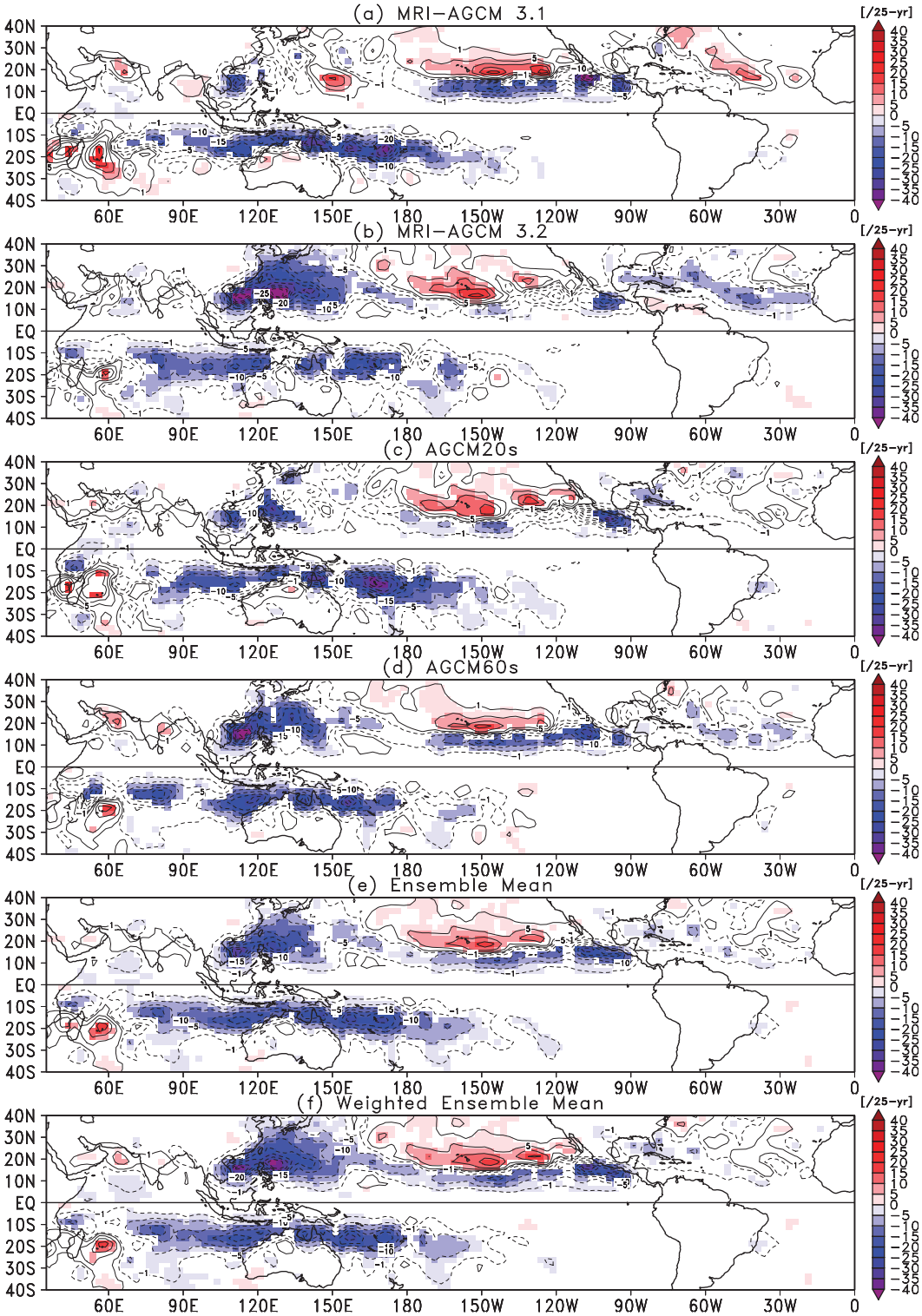

FIG. 9. Projected future changes in TCF (number per 25 yr) during the peak TC season from the ensemble mean of (a) version 3.1 models (AGCM20_3.1 and AGCM60_3.1), (b) version 3.2 models (AGCM20_3.2 and AGCM60_3.2), (c) AGCM20 models (AGCM20_3.1 and AGCM20_3.2), (d) AGCM60 models (AGCM60_3.1 and AGCM60_3.2), (e) all the models, and (f) all the models using the weighting function given by Eq. (1) (see text). Solid contours indicate positive changes, and broken contours indicate negative changes. Shaded areas indicate a 90% or greater confidence level (two-sided Student's *t* test).

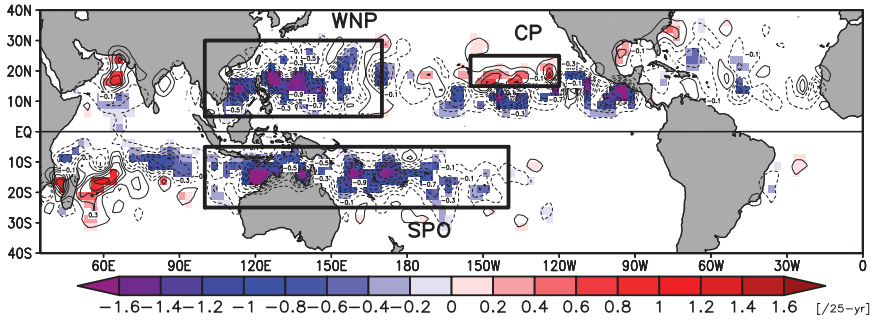

FIG. 10. As in Fig. 9f, but for projected future changes in TGF.

Both ensemble means (Figs. 9e,f) show significant decreases in TCF in the SPO and in the WNP, while significant increases in TCF are shown in the CP. These changes are similar to the projected changes in TGF in these regions (Fig. 10), indicating that the TCF changes are primarily controlled by the TGF changes. The mechanisms responsible for these future changes in TGF will be discussed in section 5.

c. *TC intensity*

The AGCM20_3.1 GW simulation projects both a significant decrease in the frequency of weak TCs and a significant increase in the frequency of intense TCs (Figs. 8a–f). In contrast, AGCM20_3.2 projects a weaker increase in the frequency of intense TCs globally (Figs. 8g,j); however, it does not show a clear future increase in TC intensity in the SH (Figs. 8i,l). Table 4 lists the observed and projected mean maximum surface wind speed and the lifetime maximum surface wind speed, along with their future changes projected by AGCM20_3.1 and AGCM20_3.2. AGCM20_3.1 projects a significant future increase in mean TC intensity for all basins (Table 4b), while AGCM20_3.2 projects a significant future increase for most of the basins (Table 4c), although to a smaller degree than that projected by AGCM20_3.1; however, AGCM20_3.2 projects a significant weakening of TC intensity in the SPO for both mean and lifetime maximum surface wind speeds (Tables 4c,f).

Figure 11 shows the spatial distributions of the mean maximum surface wind speed. Although AGCM20_3.1 (Fig. 11a) underestimates and AGCM20_3.2 (Fig. 11d) overestimates the mean TC intensity compared with observations (Fig. 11g), the versions show different spatial distributions in projected future changes (Figs. 11c,f). For example, AGCM20_3.1 projects large increases in mean TC intensity over the eastern WNP (Fig. 11c), while AGCM20_3.1 projects a striped pattern throughout the WNP. Moreover, the two versions project different future changes in the SPO: AGCM20_3.1 projects an increase in mean TC intensity, whereas AGCM20_3.2 projects a marked decrease. The spatial patterns in SIO and NAT are consistent between the models; however, the degree of future change and the location of the maximum future change are different.

Figures 11h,i show the spatial pattern of future changes in the MPI (Emanuel 1995; Bister and Emanuel 1998), as projected by the two versions. The results highlight the inconsistent nature of future changes compared with the mean maximum wind speed. The reason for this inconsistency remains unclear. Because the MPI is determined by the maximum entropy difference between the cyclone center and the environment, it is highly sensitive to the choice of environmental parameters, such as the environmental relative humidity (Holland 1997; Camp and Montgomery 2001). However, the present analyses revealed that SST change is responsible for the MPI change because relative humidity in the SPO shows a slight decrease in the future projections (see Fig. 13f, as discussed in section 5). Tang and Emanuel (2010) suggest that midlevel ventilation induced by vertical wind shear has a detrimental effect on TC intensity by decreasing the maximum steady-state intensity significantly below the potential intensity. Incorporating the effect of vertical wind shear into the MPI may help to capture the projected future decrease in the mean TC intensity because the projected vertical wind shear shows a significant increase in the SPO (see Fig. 13e, as discussed in section 5). Further analysis is needed to address this issue.

A possible reason for the smaller future increase in the frequency of intense TCs projected by AGCM20_3.2 (Figs. 8g–l) compared with AGCM20_3.1 (Figs. 8a–f) is that the maximum TC intensity resolvable at 20-km resolution has already been attained in the AGCM20_3.2 PD simulation, because a resolution of 20 km may be insufficient to fully resolve all of the observed intense TCs. Table 4 indicates that AGCM20_3.2 shows smaller fractional future increases in TC intensity compared with AGCM20_3.1, even in the ocean basins in which both versions show positive future changes. If this is the case, then AGCM20_3.2 may not be able to produce more

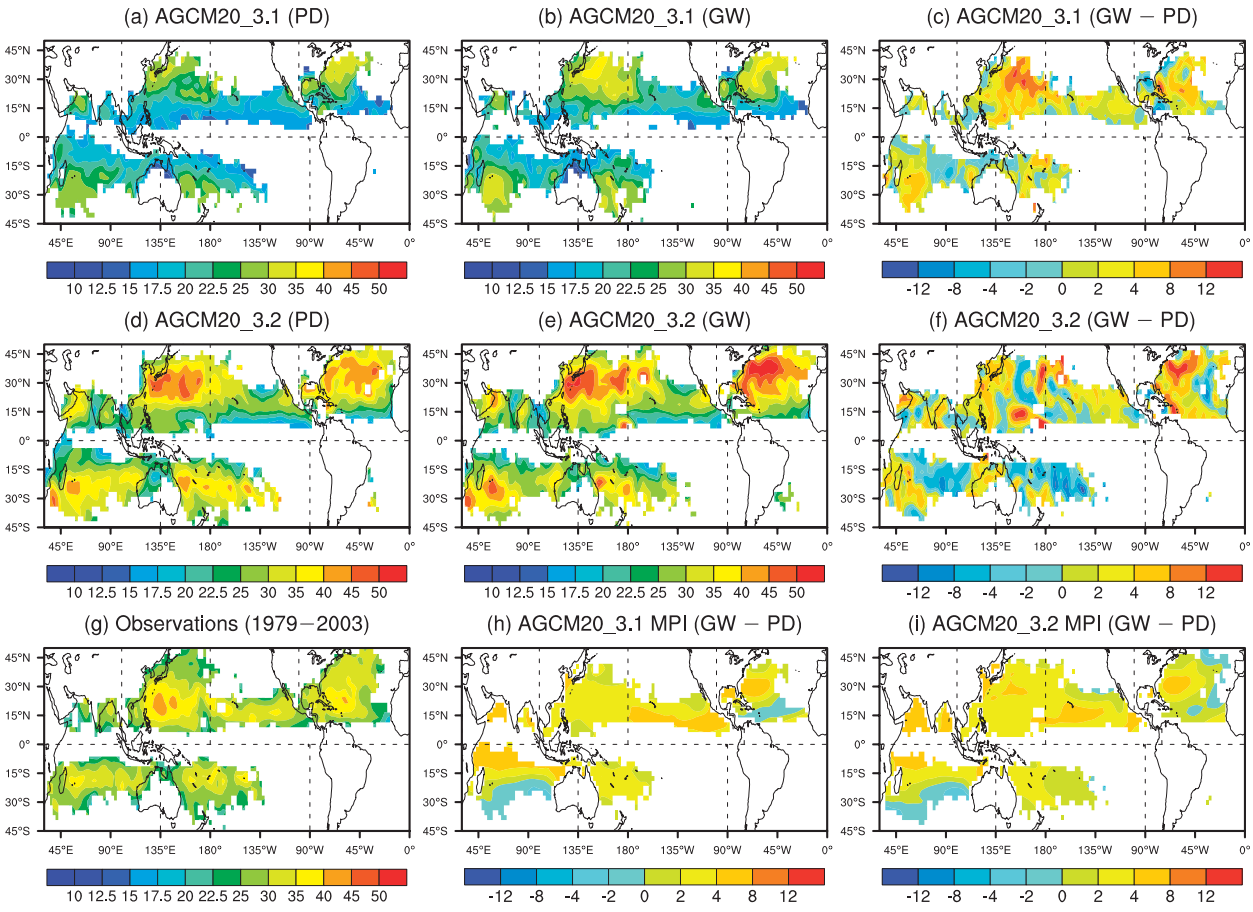

FIG. 11. Spatial distribution of mean TC intensity (m s^{-1}) simulated using AGCM20_3.1 for the (a) PD simulation, (b) GW projection, and (c) projected future changes. (d)–(f) As in (a)–(c), but using AGCM20_3.2. (g) Observed distribution (1979–2003). (h),(g) Future changes in MPI (m s^{-1}) (Emanuel 1995; Bister and Emanuel 1998) during the peak TC season, as simulated by AGCM20_3.1 and AGCM20_3.2, respectively.

intense TCs in the GW simulation. This explanation is only a conjecture and needs to be carefully investigated in the future. The relationship between maximum wind speed and minimum SLP of individual TCs simulated in the GW runs follows the same curve as the one simulated in the PD runs (Figs. 7a,b), although there are more points representing extremely intense TCs. This result suggests that the relationship between maximum wind speed and minimum SLP does not change with global warming, in agreement with the results reported in Oouchi et al. (2006) and Murakami and Sugi (2010).

In summary, despite a projected global decrease in the TC genesis number, the frequency of intense TCs is projected to increase under global warming; however, the new version of the model shows a small increase in the frequency of intense TCs at the global scale. This result arises partly because the projected mean TC intensity shows significant decreases in the SPO in the new version of the model. According to Knutson et al. (2010a), previous studies have also reported projected weakening of TC intensity in the SPO in a warmed climate (e.g., Oouchi et al. 2006; Vecchi and Soden 2007c; Emanuel et al. 2008); however, other studies have reported a marked increase in projected TC intensity within this basin (Walsh et al. 2004; Leslie et al. 2007). These regional discrepancies are indicative of the continuing uncertainties regarding how TC intensity (as well as TC frequency) is likely to change at the basin scale.

d. TCs approaching land

A reliable assessment of possible future changes in the frequency of TC landfalls is important for projecting future TC-related socioeconomic losses. This study emulates the analysis used by Murakami et al. (2012) to assess the projected changes in the frequency of TC landfalls simulated by the AGCM. The statistics of frequency of TC landfalls is calculated for TCs located within 200 km of the coast, where the coast is represented

TABLE 5. Annual mean TC storm days, defined as the number of days in all seasons when a tropical cyclone is within 200 km of the coast, for each ocean basin. Observations (1979–2003) and equally weighted ensemble mean of the PD simulations (1979–2003) and the GW projections (2075–99), and projected future change (%). Bold numbers indicate that the projected future change is statistically significant at the 99% level (two-sided Student's *t* test).

	Observations	PD	GW	GW − PD
GL	77.7	79.0	62.0	**−21.5**
NH	56.8	44.9	33.9	**−24.5**
SH	20.9	34.0	28.1	**−17.5**
NIO	4.9	9.6	8.8	−8.4
WNP	34.0	25.6	16.7	**−35.0**
ENP	5.8	3.7	3.6	−2.7
NAT	12.2	5.9	4.8	−18.7
SIO	12.2	21.7	20.5	−5.4
SPO	8.7	12.4	7.6	**−38.5**

by the outer edge of the model's land surface grid cells. Table 5 lists the observed and equally weighted ensemble mean counts of annual mean storm days, which are calculated as the TC frequency derived from the 6-hourly data divided by 4 for the periods when TCs are located in the coastal regions. The PD simulation agrees reasonably well with observations in most coastal regions, although it underestimates storm days in the NAT and overestimates storm days in the NIO, SIO, and SPO. The number of storm days is projected to decrease in all regions under global warming, with particularly large reductions projected in coastal regions of the WNP (35% decrease) and SPO (39% decrease).

Taking the average instantaneous maximum surface wind speeds of TCs in coastal regions as a measure of intensity, TCs in coastal regions intensify in all ocean basins (1%–7% increase; Table 6). This result is consistent with the results in Murakami et al. (2012), Yu and Wang (2009), and Yu et al. (2010), indicating that TC landfall events may become increasingly severe as climate warms even though the frequency of TC landfall events is projected to decrease. For example, the AGCM20_3.2 GW simulation projects an increase in the frequency of extremely intense TCs of C5 on the Saffir–Simpson scale (i.e., maximum surface winds $>$ 70 m s^{-1}). Figure 12 shows the observed and the simulated TCF of C5 TCs. The frequency of C5 TCs appears to increase in the northern portion of the WNP basin under global warming (Fig. 12e), giving rise to the potential for an increase in catastrophic damage caused by TCs in the region. Note that the tracks of C5 TCs in the AGCM20_3.2 PD simulation (Fig. 12b) show a northward shift (Fig. 12d) relative to observations (Fig. 12a). This bias should be taken into account and corrected when interpreting the results.

TABLE 6. As in Table 5, but for the average instantaneous maximum surface wind speed (m s^{-1}) TCs within 200 km of the coast.

	Observations	PD	GW	GW − PD
GL	30.5	20.8	21.8	**5.2**
NH	31.1	21.7	22.8	**5.5**
SH	29.0	19.5	20.6	**5.7**
NIO	28.8	20.2	21.4	**6.0**
WNP	31.5	22.3	23.7	**6.5**
ENP	29.7	20.5	21.9	**6.8**
NAT	31.5	21.1	21.5	1.8
SIO	29.2	19.5	20.9	**7.0**
SPO	28.6	19.7	20.0	1.4

5. Discussion

This section discusses the mechanisms responsible for the projected future changes in TC genesis frequency. Murakami and Wang (2010) and Murakami et al. (2012) used a modified version of the genesis potential index (GPI) to investigate the factors that contribute to the projected future changes in their simulations. The modified GPI comprises five large-scale dynamical and thermodynamic factors: vorticity at 850 hPa (η_{850}), relative humidity at 700 hPa (RH_{700}), the MPI defined by Emanuel (1995) and Bister and Emanuel (1998), the vertical wind shear between 850 and 200 hPa (V_s), and vertical velocity at 500 hPa (ω_{500}). Yokoi and Takayabu (2009) and Li et al. (2010) also attributed the projected future changes in TGF to changes in the variance of TSDs, in addition to changes in the GPI. Figure 13 shows the projected future changes of each factor according to the equally weighted ensemble mean. As was done before, grid cells in which the monthly-mean TCF value is more than 3.0 have been removed prior to computing the climatological mean fields, to reduce the influence of TCs on the mean.

Among the factors plotted in Fig. 13, the distribution of the projected changes in TSD (Fig. 13a) is most highly correlated with the distribution of the projected changes in global TGF (Fig. 10). The projected changes in TSD are consistent with those reported by Yokoi and Takayabu (2009), Li et al. (2010), and Murakami et al. (2011). The decreased occurrence of TSDs over the WNP and SPO appears to stem from the local suppression of upward motion, while the increased occurrence of TSDs over the CP appears to originate from the local enhancement of upward motion (Fig. 13c). These dynamical changes are associated with a weakening of the Walker circulation (Vecchi and Soden 2007b), as described below.

The second and third most highly correlated factors are the dynamical parameters η_{850} and ω_{500} (Figs. 13b,c), indicating that changes in these dynamical variables are

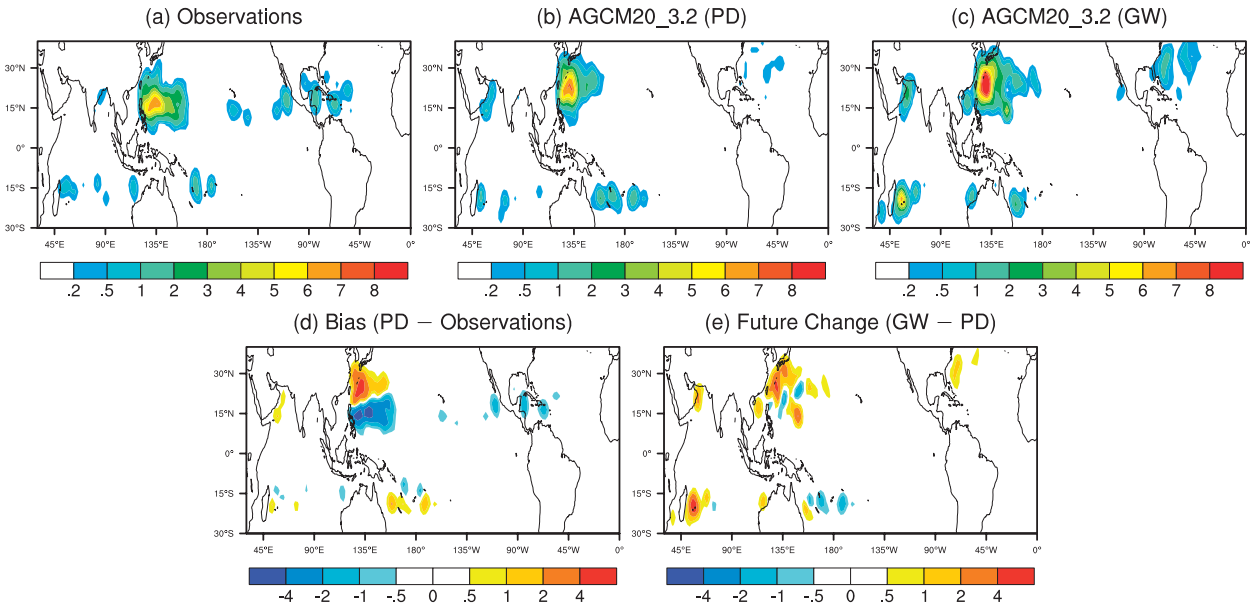

FIG. 12. TCF (number per 25 yr) of C5 TCs during all seasons for (a) observations (1979–2003), (b) PD simulation (1979–2003) using AGCM20_3.2, and (c) GW projection (2075–99) using AGCM20_3.2. (d) Difference between the PD simulation using AGCM20_3.2 and observations. (e) Projected future changes (GW − PD) using AGCM20_3.2.

also responsible for the projected global changes in TGF (see also Murakami et al. 2011). The projected changes in ω_{500} are associated with the projected weakening of the Pacific Walker circulation: upward motion decreases in the predominantly ascending branch of the Walker circulation over the WNP and SPO, while upward motion increases in the predominantly subsiding branch over the CP. Applying the analysis introduced by Vecchi and Soden (2007b), the mean rate of the decrease in the upward ω_{500} is about 2.5% for all the models and the spatial variance of ω_{500} within the tropics (30°S–30°N) decreases by about 9.3%. Almost 97% of this decrease is due to a weakening of the zonally asymmetric component of the tropical circulation (i.e., Walker circulation; see Fig. 13c), with the remainder due to a slight weakening of the zonally symmetric component (i.e., Hadley circulation). This result is consistent with previous studies (e.g., Vecchi and Soden 2007b; Murakami et al. 2012). The projected changes in the spatial pattern of η_{850} appear to be associated with the projected changes in the spatial pattern of ω_{500}. Murakami et al. (2012) found that cyclonic vorticity increases in the southeastern quadrant of the WNP in response to global warming, and they suggested that this results from the Rossby wave response (Gill 1980) to equatorially antisymmetric heating (as expressed in upward motion) over the CP. Similar responses can be seen in other basins: cyclonic vorticity anomalies appear at the northwest (southwest) flank of upward motion anomalies in the NH (SH).

The MPI and RH_{700} are less correlated with the global changes in TGF (Figs. 13d,f). These relatively weak correlations indicate that the thermodynamic factors are of secondary importance to the projected global changes in TGF (see also Murakami et al. 2011). However, in the three regions with the projected significant future changes (WNP, CP, and SPO), the changes in thermodynamic factors are adequate to characterize the local changes in TGF. When compared with the surrounding areas, RH_{700} increases in the CP but decreases in the SPO (note that the sign of projected changes in TGF is opposite to that of RH_{700} in the WNP), while the MPI increases substantially in the CP but increases only slightly in the WNP and SP. The changes in the MPI correspond directly to the changes in the spatial distribution of local SST (Fig. 2). The MPI shows a marked increase at locations where the local SST increases substantially, while it shows a slight increase or even a decrease at locations where the SST shows a slight increase, which is consistent with the results of Vecchi and Soden (2007a,c). Future changes in the spatial pattern of precipitation (Figs. 1e,f) also correspond to changes in the spatial pattern of SST. For example, precipitation increases substantially in the equatorial Indian Ocean, tropical Atlantic, and CP, where SST also increases substantially. The future change in global mean precipitation is approximately $+0.25$ mm day^{-1}, and this increase is larger in the NH (approximately $+0.30$ mm day^{-1}) than in the SH (approximately $+0.20$ mm day^{-1}). This hemispheric asymmetric change in precipitation reflects the fact that the prescribed changes

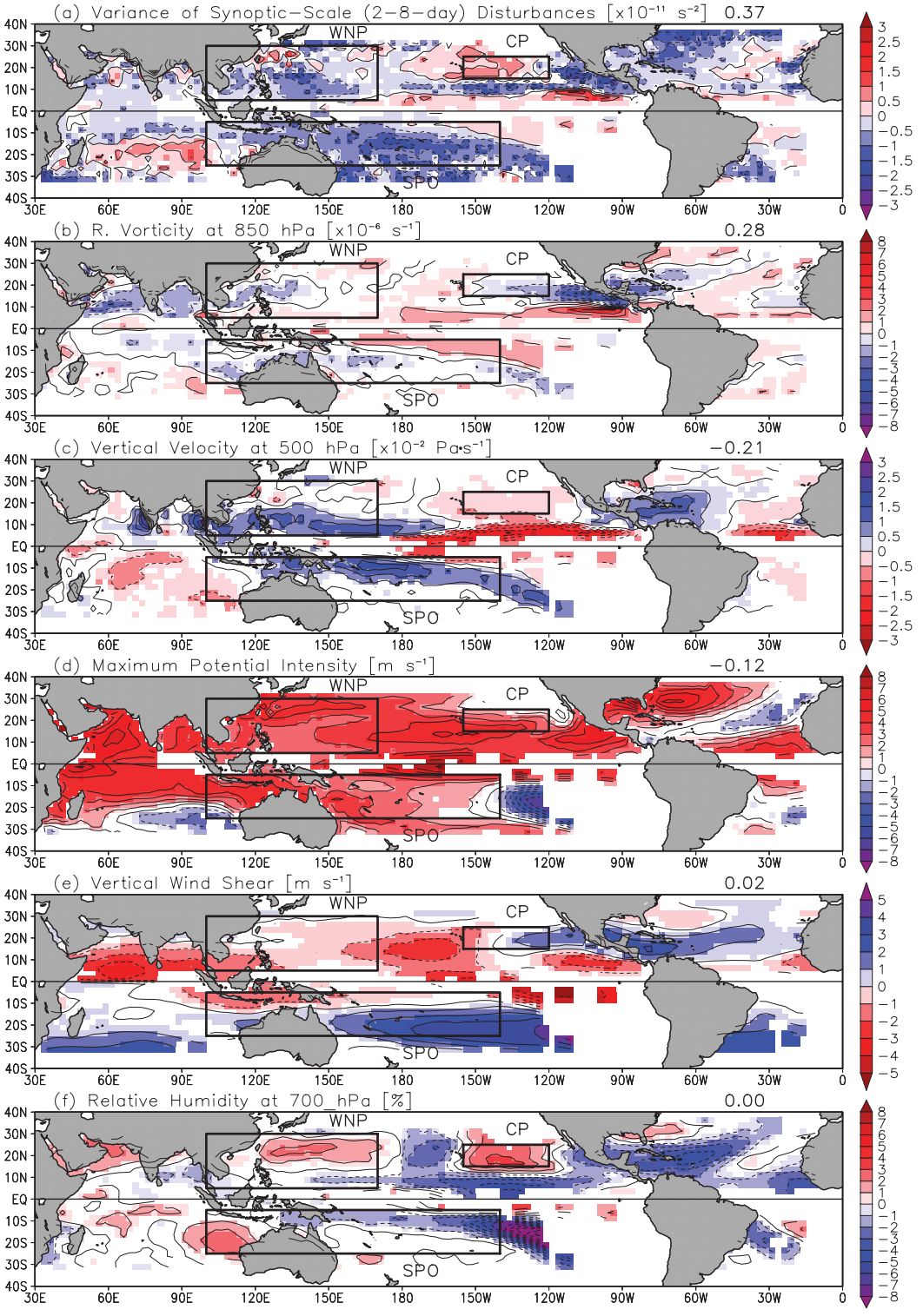

FIG. 13. Weighted ensemble mean of projected future changes in the (a) variance of synoptic-scale (2−8 days) vorticity at 850 hPa (10^{-11} s^{-2}), (b) vorticity at 850 hPa (10^{-6} s^{-1}), (c) vertical p velocity at 500 hPa (10^{-2} Pa s^{-1}), (d) MPI (m s^{-1}), (e) vertical wind shear between 850 and 200 hPa (m s^{-1}), and (f) relative humidity at 700 hPa (%). Solid contours indicate positive changes, and broken contours indicate negative changes. Shaded areas indicate a 90% or greater confidence level (two-sided Student's t test). Boxes define the boundaries of the WNP, CP, and SPO regions discussed in the text. The number at top right in each panel shows the spatial correlation coefficient between the plotted quantity and the projected changes in TGF shown in Fig. 10.

in SST show a greater warming in the NH than in the SH (Fig. 2).

Among the factors plotted in Fig. 13, global changes in V_s (Fig. 13e) are little correlated with the global changes in the TGF. In particular, the signs of the projected changes in V_s are inconsistent with changes in the TGF in the WNP and CP. Although the spatial pattern of changes in V_s is similar to that reported by Vecchi and Soden (2007c), who used the future projections of 22 CMIP3 models under the A1B scenario, the results shown in Fig. 13e suggest that changes in V_s may only affect the TGF in the NAT and SPO.

Based on these results, the projected future changes in TC activity may be attributed to changes in the tropical overturning circulation, as well as to local and remote effects of SST. The projected reductions in global and hemispheric TCF appear to be caused by a weakening of the tropical overturning circulation, especially the Walker circulation. This projected weakening of the overturning circulation appears to be independent of the differences in model physics between versions 3.1 and 3.2. The local effects consist of the primary responses to local SST anomalies. Changes in the local SST anomalies are the key to the changes in local convective activity (precipitation) and synoptic-scale disturbances, which in turn determine changes in the frequency of local TC genesis and occurrence. The remote effects consist of the Rossby wave response, anomalies in vertical motion, and vertical wind shear that are induced by remote convective activity. Both local and remote effects appear to be sensitive to the differences in the model physics. The relative importance of each effect may differ from basin to basin, leading to differences in the projected basin-scale changes in TC activity in models with different physics.

6. Summary

Climate simulations of the present-day (1979–2003, PD) and of the end of the twenty-first century (2075–99, GW) under the IPCC A1B scenario were conducted using the new version of the MRI-AGCM (version 3.2) to investigate possible future changes in TC activity at global and regional scales. Simulations were conducted using two different resolutions (20 and 60 km) of version 3.2 along with identical configurations of a previous version of the MRI-AGCM3.1 (version 3.1) to evaluate uncertainties caused by differences in the model resolution and model physics.

Results for the PD simulation demonstrate that version 3.2 reproduces the climatological mean spatial distribution of the global TCs more realistically than version 3.1. In particular, version 3.2 reduces biases in the number of the simulated TCs in the western North Pacific (low bias) and Southern Hemisphere (high bias) and yields a more reasonable present-day global distribution of TCs. These improvements appear to result from concurrent improvements in the simulation of the large-scale vorticity and vertical velocity fields, which are consistent with improvements in the simulation of precipitation. Although the skill of version 3.2 in simulating the interannual variation of TC number is not improved relative to version 3.1, the seasonal cycle of global TC genesis number is improved considerably. The distribution of TC intensity simulated by version 3.2 is also comparable to observations. Specifically, the 20-km-mesh model version 3.2 is able to simulate extremely intense TCs (categories 4 and 5 with maximum surface wind speed of more than 59 m s^{-1}) reasonably well compared with observations. We would like to emphasize that this study represents the first result that a global climate model has successfully simulated such intense TCs through multidecadal simulations. The improvements in TC intensity are due to the use of a new cumulus convection scheme in version 3.2. The version 3.2 model also simulates reasonable TC structures while retaining the observed relationship between the maximum surface wind speed and the minimum sea level pressure for all TCs, indicating that the model has the potential to simulate reasonable TC structures even in the case of extremely intense TCs. These improvements in simulating the present-day TC climatology instill greater confidence in projections of potential future climate change of TC activity.

Global and hemispheric TC genesis numbers are projected to decrease significantly (13%–25%) under the GW scenario regardless of the model version or resolution. Moreover, all models project significant decreases in the number of TCs in the western North Pacific (WNP), South Indian Ocean (SIO), and South Pacific Ocean (SPO), although the projected changes in the North Atlantic (NAT) and eastern North Pacific (ENP) are inconsistent among the models. The projected future changes in the TC frequency of occurrence (TCF) show large spatial variation: a significant decrease in the WNP and SPO and a significant increase in the central Pacific (CP).

Both versions 3.2 and 3.1 project a statistically significant increase in the frequency of intense TCs with global warming. However, the increase is smaller in v3.2 than in v3.1. This difference between the models arises partly because version 3.2 projects a significant future decrease in TC intensity over the SPO. The frequency of TCs approaching coastal regions decreases over the WNP (by 35%) and over the SPO (by 39%); however, version 3.2 projects a future increase in the frequency of category 5 TCs in the northern portion of the WNP. When the

instantaneous maximum surface wind velocities for TCs are averaged, all coastal regions show an increasing intensity by 1%-7%. These results indicate that TC-related socioeconomic damage may become more severe under global warming, particularly in the northern portion of the WNP, even though the frequency of TCs approaching coastal regions is projected to decrease.

A weighting method that takes the model biases into account when calculating the ensemble mean has also been proposed. The qualitative nature of the results obtained by this method is similar to that of the results obtained by an equal weighting for all the models. The projected changes in TC genesis frequency (TGF) are similar to the projected changes in TCF. A number of dynamical and thermodynamic background fields have been examined to determine the contributions to the projected future changes in TGF. Among them, the projected changes in the variance of tropical synoptic-scale disturbances (TSDs) are most highly correlated with the projected changes in TGF. The second and third most highly correlated factors are relative vorticity at 850 hPa and vertical velocity at 500 hPa; both of these changes are associated with the projected weakening of the Walker circulation.

Global and hemispheric TGFs are consistently projected to decrease significantly under global warming, but some projected regional changes in TC activity differ with different model versions. Varying results are also obtained in terms of the degree and even the sign of future changes in mean TC intensity for individual basins. These regional discrepancies underscore a continuing uncertainty regarding the characteristics of the local and basin-scale changes in TC activity. Moreover, neither the sensitivity of the results to the choice of global warming scenario nor the sensitivity of the results to the spatial pattern of SST changes has been constrained in this study. Multimodel, multiscenario, and multi-SST ensemble realizations are necessary for more reliable projections of future TC activity. The results from this study show that the projected changes in TC activity are consistent between the 20- and 60-km-resolution simulations. It would therefore be worthwhile to more fully explore the uncertainties in the projections of future changes in TC activity using coarse-resolution models, given the fact that the current use of high-resolution global models remains computationally too expensive.

Acknowledgments. This work was conducted under the framework of the Projection of the Change in Future Weather Extremes Using Super-High-Resolution Atmospheric Models project supported by the KAKUSHIN program of the Ministry of Education, Culture, Sports, Science and Technology (MEXT) of Japan. HM would like to thank the IPRC for supporting his visit to the IPRC and to thank Prof. Tim Li for his useful comments and suggestions. YW is supported in part by NSF Grant ATM-0754039. Calculations were performed on the Earth Simulator.

REFERENCES

Alley, R., and Coauthors, 2007: Summary for policymakers. *Climate Change 2007: The Physical Science Basis,* S. Solomon et al., Eds., Cambridge University Press, 1–18.

Arakawa, A., and W. H. Schubert, 1974: Interaction of cumulus cloud ensemble with the large-scale environment. Part I. *J. Atmos. Sci.,* **31,** 674–701.

Atkinson, G. D., and C. R. Holiday, 1977: Tropical cyclone minimum sea level pressure/maximum sustained wind relationship for the western North Pacific. *Mon. Wea. Rev.,* **105,** 421–427.

Bengtsson, L., M. Botzet, and M. Esch, 1996: Will greenhouse gas-induced warming over the next 50 years lead to higher frequency and greater intensity of hurricanes? *Tellus,* **48A,** 57–73.

——, K. I. Hodges, M. Esch, N. Keenlyside, L. Kornblueh, J.-J. Luo, and T. Yamagata, 2007: How may tropical cyclones change in a warmer climate? *Tellus,* **59A,** 539–561.

Bister, M., and K. A. Emanuel, 1998: Dissipative heating and hurricane intensity. *Meteor. Atmos. Phys.,* **52,** 233–240.

Camp, J. P., and M. T. Montgomery, 2001: Hurricane maximum intensity: Past and present. *Mon. Wea. Rev.,* **129,** 1704–1717.

Ding, Y., and D. R. Sikka, 2006: Synoptic systems and weather. *The Asian Monsoon,* B. Wang, Ed., Springer, 131–201.

Emanuel, K. A., 1987: The dependence of hurricane intensity on climate. *Nature,* **326,** 483–485.

——, 1995: Sensitivity of tropical cyclones to surface exchange coefficients and a revised steady-state model incorporating eye dynamics. *J. Atmos. Sci.,* **52,** 3969–3976.

——, R. Sundararajan, and J. Williams, 2008: Hurricanes and global warming: Results from downscaling IPCC AR4 simulations. *Bull. Amer. Meteor. Soc.,* **89,** 347–367.

Frank, W. M., 1984: A composite analysis of the core of a mature hurricane. *Mon. Wea. Rev.,* **112,** 2401–2420.

Gill, A. E., 1980: Some simple solutions for heat-induced tropical circulation. *Quart. J. Roy. Meteor. Soc.,* **106,** 447–462.

Gualdi, S., E. Scoccimarro, and A. Navarra, 2008: Changes in tropical cyclone activity due to global warming: Results from a high-resolution coupled general circulation model. *J. Climate,* **21,** 5204–5228.

Hawkins, H. F., and D. T. Rubsam, 1968: Hurricane Hilda, 1964. II. Structure and budgets of the hurricane on October 1, 1964. *Mon. Wea. Rev.,* **96,** 617–636.

Holland, G. J., 1997: The maximum potential intensity of tropical cyclones. *J. Atmos. Sci.,* **54,** 2519–2541.

Kitoh, A., T. Ose, K. Kurihara, S. Kusunoki, M. Sugi, and KAKUSHIN Team-3 Modeling Group, 2009: Projection of changes in future weather extremes using super-high-resolution global and regional atmospheric models in the KAKUSHIN program: Results of preliminary experiments. *Hydrol. Res. Lett.,* **3,** 49–53.

Knutson, T. R., and Coauthors, 2010a: Tropical cyclones and climate change. *Nat. Geosci.,* **3,** 157–163.

——, C. W. Landsea, and K. A. Emanuel, 2010b: Tropical cyclones and climate change: A review. *Global Perspectives on Tropical Cyclones: From Science to Mitigation,* J. C. L. Chan and J. D. Kepert, Eds., World Scientific Series on Asia-Pacific Weather and Climate, Vol. 4, World Scientific Publishing Company, 243–284.

LaRow, T. E., Y.-K. Lim, D. W. Shin, E. P. Chassignet, and S. Cocke, 2008: Atlantic basin seasonal hurricane simulations. *J. Climate,* **21,** 3191–3206.

Lau, K.-H., and N.-C. Lau, 1990: Observed structure and propagation characteristics of tropical summertime synoptic-scale disturbances. *Mon. Wea. Rev.,* **118,** 1888–1913.

Leslie, L. M., D. J. Karoly, M. Leplastrier, and B. W. Buckley, 2007: Variability of tropical cyclones over the southwest Pacific Ocean using a high-resolution climate model. *Meteor. Atmos. Phys.,* **97,** 171–180.

Li, T., M. Kwon, M. Zhao, J.-S. Kug, J.-J. Luo, and W. Yu, 2010: Global warming shifts Pacific tropical cyclone location. *Geophys. Res. Lett.,* **37,** L21804, doi:10.1029/2010GL045124.

Liu, P., and Coauthors, 2009: Tropical intraseasonal variability in the MRI-20km60L AGCM. *J. Climate,* **22,** 2006–2022.

Madden, R. A., and P. R. Julian, 1972: Description of global-scale circulation cells in the tropics with a 40–50 day period. *J. Atmos. Sci.,* **29,** 1109–1123.

——, and ——, 1994: Observations of the 40–50-day tropical oscillation—A review. *Mon. Wea. Rev.,* **122,** 814–837.

Mizuta, R., and Coauthors, 2006: 20-km-mesh global climate simulations using JMA-GSM model–mean climate states. *J. Meteor. Soc. Japan,* **84,** 165–185.

——, Y. Adachi, S. Yukimoto, and S. Kusunoki, 2008: Estimation of the future distribution of sea surface temperature and sea ice using the CMIP3 multi-model ensemble mean. Meteorological Research Institute Tech. Rep. 56, 28 pp. [Available online at http://www.mri-jma.go.jp/Publish/Technical/DATA/VOL_56/56_en.html.]

——, and Coauthors, 2012: Climate simulations using MRI-AGCM with 20-km grid. *J. Meteor. Soc. Japan,* **90A,** 235–260.

Murakami, H., and M. Sugi, 2010: Effect of model resolution on tropical cyclone climate projections. *SOLA,* **6,** 73–76.

——, and B. Wang, 2010: Future change of North Atlantic tropical cyclone tracks: Projection by a 20-km-mesh global atmospheric model. *J. Climate,* **23,** 2699–2721.

——, T. Matsumura, R. Sakai, A. Noda, and S. Kusunoki, 2008: Verification of typhoon forecasts for a 20 km-mesh high-resolution global model. *J. Meteor. Soc. Japan,* **86,** 669–698.

——, B. Wang, and A. Kitoh, 2011: Future change of western North Pacific typhoons: Projections by a 20-km-mesh global atmospheric model. *J. Climate,* **24,** 1154–1169.

——, R. Mizuta, and E. Shindo, 2012: Future changes in tropical cyclone activity projected by multi-physics and multi-SST ensemble experiments using the 60-km-mesh MRI-AGCM. *Climate Dyn.,* doi:10.1007/s00382-011-1223-x, in press.

Oouchi, K., J. Yoshimura, H. Yoshimura, R. Mizuta, S. Kusunoki, and A. Noda, 2006: Tropical cyclone climatology in a global-warming climate as simulated in a 20 km-mesh global atmospheric model: Frequency and wind intensity analysis. *J. Meteor. Soc. Japan,* **84,** 259–276.

Rajendran, K., A. Kitoh, R. Mizuta, S. Jajani, and T. Nakazawa, 2008: High resolution simulation of mean convection and its intraseasonal variability over the tropics in MRI/JMA 20-km mesh AGCM. *J. Climate,* **21,** 3722–3739.

Randall, D., and D.-M. Pan, 1993: Implementation of the Arakawa-Schubert cumulus parameterization with a prognostic closure. *The Representation of Cumulus Convection in Numerical Models, Meteor. Monogr.,* No. 46, Amer. Meteor. Soc., 137–144.

Rayner, N. A., D. E. Parker, E. B. Horton, C. K. Folland, L. V. Alexander, and D. P. Rowell, 2003: Global analysis of sea surface temperature, sea ice, and night marine air temperature since the late nineteenth century. *J. Geophys. Res.,* **108,** 4407, doi:10.1029/2002JD002670.

Solomon, S., D. Qin, M. Manning, M. Marquis, K. Averyt, M. M. B. Tignor, H. L. Miller Jr., and Z. Chen, Eds., 2007: *Climate Change 2007: The Physical Science Basis.* Cambridge University Press, 996 pp.

Stowasser, M., Y. Wang, and K. Hamilton, 2007: Tropical cyclone changes in the western North Pacific in a global warming scenario. *J. Climate,* **20,** 2378–2396.

Sugi, M., A. Noda, and N. Sato, 2002: Influence of the global warming on tropical cyclone climatology. *J. Meteor. Soc. Japan,* **80,** 249–272.

——, H. Murakami, and J. Yoshimura, 2009: A reduction in global tropical cyclone frequency due to global warming. *SOLA,* **5,** 164–167.

Tang, B., and K. Emanuel, 2010: Midlevel ventilation's constraint on tropical cyclone intensity. *J. Atmos. Sci.,* **67,** 1817–1830.

Taylor, K. E., 2001: Summarizing multiple aspects of model performance in a single diagram. *J. Geophys. Res.,* **106** (D7), 7183–7192.

Tiedtke, M., 1989: Acomprehensive mass flux scheme for cumulus parameterization in large-scale models. *Mon. Wea. Rev.,* **117,** 1779–1800.

Unisys, cited 2011: Unisys weather hurricane/tropical data. [Available online at http://weather.unisys.com/hurricane/.]

Vecchi, G. A., and B. J. Soden, 2007a: Effect of remote sea surface temperature change on tropical cyclone potential intensity. *Nature,* **450**, 1066–1070.

——, and ——, 2007b: Global warming and the weakening of the tropical circulation. *J. Climate,* **20,** 4316–4340.

——, and ——, 2007c: Increased tropical Atlantic wind shear in model projections of global warming. *Geophys. Res. Lett.,* **34,** L08702, doi:10.1029/2006GL028905.

Walsh, K. J. E., K.-C. Nguyen, and J. L. McGregor, 2004: Fine-resolution regional climate model simulations of the impact of climate change on tropical cyclones near Australia. *Climate Dyn.,* **22,** 47–56.

——, M. Fiorino, C. W. Landsea, and K. L. McInnes, 2007: Objectively determined resolution-dependent threshold criteria for the detection of tropical cyclones in climate models and reanalyses. *J. Climate,* **20,** 2307–2314.

Xie, P., and P. A. Arkin, 1997: Global precipitation: A 17-year monthly analysis based on gauge observations, satellite estimates, and numerical model outputs. *Bull. Amer. Meteor. Soc.,* **78,** 2539–2558.

Xie, S.-P., C. Deser, G. A. Vecchi, J. Ma, H. Teng, and A. T. Wittenberg, 2010: Global warming pattern formation: Sea surface temperature and rainfall. *J. Climate,* **23,** 966–986.

Yokoi, S., and Y. N. Takayabu, 2009: Multi-model projection of global warming impact on tropical cyclone genesis frequency over the western North Pacific. *J. Meteor. Soc. Japan,* **87,** 525–538.

——, ——, and J. C. L. Chan, 2009: Tropical cyclone genesis frequency over the western North Pacific simulated in

medium-resolution coupled general circulation models. *Climate Dyn.,* **33,** 665–683.

Yu, J., and Y. Wang, 2009: Response of tropical cyclone potential intensity over the north Indian Ocean to global warming. *Geophys. Res. Lett.,* **36,** L03709, doi:10.1029/2008GL036742.

——, ——, and K. Hamilton, 2010: Response of tropical cyclone potential intensity to a global warming scenario in the IPCC AR4 CGCMs. *J. Climate,* **23,** 1354–1373.

Yukimoto, S., and Coauthors, 2011: Meteorological Research Institute-Earth System Model version 1 (MRI-ESM1)—Model description. Meteorological Research Institute Tech. Rep. 64, 88 pp. [Available online at http://www.mri-jma.go.jp/Publish/Technical/DATA/VOL_64/index.html.]

Zhao, M., I. M. Held, S.-J. Lin, and G. A. Vecchi, 2009: Simulations of global hurricane climatology, interannual variability, and response to global warming using a 50-km resolution GCM. *J. Climate,* **22,** 6653–6678.